Editors' Suggestion

Laser-induced terahertz spin transport in magnetic nanostructures arises from the same force as ultrafast demagnetization

Reza Rouzegar,[1,2,*] Liane Brandt,[3] Lukáš Nádvorník,[1,2,4] David A. Reiss,[1] Alexander L. Chekhov,[1,2] Oliver Gueckstock,[1,2] Chihun In,[1,2] Martin Wolf,[2] Tom S. Seifert,[1] Piet W. Brouwer,[1] Georg Woltersdorf,[3] and Tobias Kampfrath[1,2,†]

[1]*Department of Physics, Freie Universität Berlin, 14195 Berlin, Germany*
[2]*Department of Physical Chemistry, Fritz Haber Institute of the Max Planck Society, 14195 Berlin, Germany*
[3]*Institut für Physik, Martin-Luther-Universität Halle, 06120 Halle, Germany*
[4]*Faculty of Mathematics and Physics, Charles University, Ke Karlovu 3, 121 16 Prague, Czech Republic*

(Received 26 May 2021; accepted 19 September 2022; published 24 October 2022)

Laser-induced terahertz spin transport (TST) and ultrafast demagnetization (UDM) are central but so far disconnected phenomena in femtomagnetism and terahertz spintronics. Here, we use broadband terahertz emission spectroscopy to reliably measure both processes in one setup. We find that the rate of UDM in a single simple ferromagnetic metal film F such as $Co_{70}Fe_{30}$ or $Ni_{80}Fe_{20}$ has the same time evolution as TST from F into an adjacent normal-metal layer N such as Pt or W. As this remarkable agreement refers to two very different samples, an F layer vs an $F|N$ stack, it does not result from the trivial fact that TST out of F reduces the F magnetization at the same rate. Instead, our observation strongly suggests that UDM in F and TST in $F|N$ are driven by the same force, which is fully determined by the state of the ferromagnet. An analytical model quantitatively explains our measurements and reveals that both UDM in the F sample and TST in the associated $F|N$ stack arise from a generalized spin voltage, i.e., an excess of magnetization, which is defined for arbitrary, nonthermal electron distributions. We also conclude that contributions due to a possible temperature difference between F and N, i.e., the spin-dependent Seebeck effect, and optical intersite spin transfer are minor in our experiment. Based on these findings, one can apply the vast knowledge of UDM to TST to significantly increase spin-current amplitudes and, thus, open promising pathways toward energy-efficient ultrafast spintronic devices.

DOI: 10.1103/PhysRevB.106.144427

I. INTRODUCTION

Fundamental operations in future spin-based electronics are the manipulation of magnetic order, the transport of spin angular momentum, and the detection of spin dynamics [1]. The research fields of femtomagnetism and terahertz spintronics aim to push the three operations to femtosecond timescales and, thus, terahertz bandwidth [1–7]. Figure 1 shows the model systems in which two key phenomena of ultrafast spin dynamics are studied extensively: a single ferromagnetic metal layer F [Fig. 1(a)] and an $F|N$ stack, where N is a normal metal layer [Fig. 1(b)].

A. Ultrafast demagnetization (UDM)

In F samples, uniform excitation by a femtosecond laser pulse induces ultrafast demagnetization [UDM; Fig. 1(a)] [2,8–12]. This effect reveals the timescales of elementary spin interactions with electron orbital and lattice degrees of freedom and is a central ingredient for ultrafast magnetization switching [3,6]. Recent experiments on ferromagnetic Fe indicate that, on a timescale of 100 fs and above, the UDM dynamics are independent of the pump photon energy and only determined by the energy the laser pulse deposits in the electronic system [13,14]. UDM is accompanied by transfer of spin angular momentum to the crystal lattice, as observed directly by ultrafast x-ray and electron diffraction probes [15,16].

Rate-equation-type theories can successfully explain UDM and involve spin flips [17,18] or magnon emission [10,19–22] due to electron scattering together with spin-orbit coupling. Alternatively, exact time propagation of small clusters [23] and time-dependent density functional theory [24] were shown to be powerful approaches to modeling UDM.

B. Terahertz spin transport (TST)

In $F|N$ stacks, uniform laser excitation not only triggers UDM but also terahertz spin transport (TST) between F and N [Fig. 1(b)] [5,6,25–30]. Such spin currents can be used to exert spin torque at ultrashort time and length scales. They may, thus, excite terahertz magnons [31–33] and, ultimately, switch

*m.rouzegar@fu-berlin.de
†tobias.kampfrath@fu-berlin.de

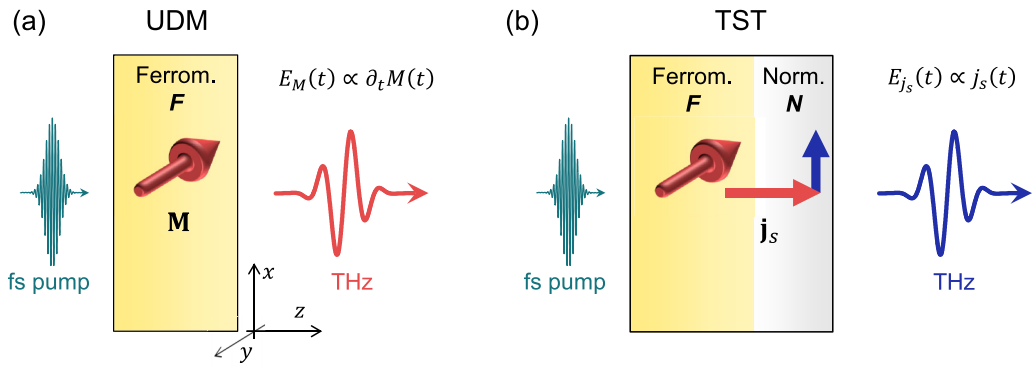

FIG. 1. Ultrafast demagnetization (UDM) vs terahertz spin transport (TST). (a) Side view of a single ferromagnetic metal layer (F) with magnetization $\mathbf{M} = M\mathbf{u}_y$ parallel to the y axis with unit vector $\mathbf{u}_y$. Excitation by a femtosecond laser pulse triggers UDM. The transient magnetic dipole gives rise to the emission of a terahertz pulse with field $E_M(t) \propto \partial_t M(t)$. (b) $F|N$ stack consisting of F and an adjacent normal paramagnetic metal layer (N). Femtosecond laser excitation drives a spin current with density $\mathbf{j}_s = j_s\mathbf{u}_z$ from F to N. In N, $\mathbf{j}_s$ is converted into a charge current with density $\mathbf{j}_c = j_c\mathbf{u}_x$, leading to the emission of a terahertz electromagnetic pulse with electric field $E_{j_s}(t) \propto j_s(t)$ directly behind the sample. Both $E_M(t)$ and $E_{j_s}(t)$ are linearly polarized perpendicular to $\mathbf{M}$ and measured by electro-optic sampling.

magnetic order [3]. TST also serves to efficiently generate broadband terahertz electromagnetic pulses for photonic and spectroscopic applications [34–47].

To understand TST, it is important to note that the optical pump promotes electrons from initial states (such as $|i\rangle$) to excited states (such as $|e\rangle$). Two different mechanisms of spin transfer from F to N can occur: shift-type and band-type transport.

The shift-type mechanism is operative when states $|i\rangle$ and $|e\rangle$ are concentrated at the $F|N$ interface and the spin polarization of $|e\rangle$ is more localized in N than that of $|i\rangle$. Optical excitation, thus, shifts spin polarization across the $F|N$ interface, like shift photocurrents of electron charge (rather than spin) in the bulk [48–50] and at the surface [51,52] of semiconductors. In magnetic heterostructures and alloys, this effect was predicted using time-dependent density functional theory calculations [53], termed optical intersite spin transfer (OISTR), and experimentally confirmed subsequently [54–57].

In contrast, band-type transport occurs if $|i\rangle$ and $|e\rangle$ are Bloch-type electron states in F that have different band velocity, lifetime, or energy. Consequently, pump excitation can lead to an imbalance in terms of electron transport across the $F|N$ interface, resulting in a flow of spin-polarized electrons from F to N. This effect is reminiscent of injection charge photocurrents in semiconductors [48,50,52]. In metallic $F|N$ structures, it was modeled using semiclassical Boltzmann-type transport equations, termed superdiffusive spin transport [58–60], and experimentally observed by optical pump-probe techniques [5,26,27,29,61] or terahertz emission spectroscopy [28,34–37,40,62].

An additional spin-current component can be triggered by excitation with circularly polarized light [63]. Its amplitude is proportional to the chirality of the pump polarization (positive, zero, or negative) and typically two orders of magnitude smaller than the bandlike component. Microscopically, this coherent effect was ascribed to an inverse spin-orbit torque [63].

C. Spin voltage

From a more macroscopic viewpoint, spin transport can, in general, be driven by spatial gradients of the parameters that determine the local electron distribution in metals, that is, electrostatic potential, temperature, and spin voltage [64,65]. While the generation of out-of-plane electrostatic-potential gradients in metallic thin films is difficult due to strong instantaneous screening [58], temperature gradients can be straightforwardly generated by ultrafast optical excitation. They are expected to result in TST through the spin-dependent Seebeck effect, which was sometimes used to rationalize the spin currents observed in previous works [31,39,40,66].

Interestingly, optical excitation of a ferromagnetic metal induces a transient excess of local spin density [61], too, which is also known as spin voltage or spin accumulation. On one hand, optically induced spin-voltage gradients were suggested to make a dominant contribution to TST [65]. On the other hand, theoretical arguments [21,67,68] indicate that the spin voltage plus temperature differences between spin-up and spin-down electrons could drive demagnetization. It follows that the seemingly disconnected phenomena of TST and UDM may share a common driving force: the spin voltage [61,69,70].

Direct experimental evidence for this exciting conjecture is, however, missing, and the relative strength of the competing Seebeck-type transport along temperature gradients and the interfacial OISTR remains unclear. Likewise, it is far from obvious whether concepts like spin voltage and temperature can be applied to nonthermal electron states that prevail in the first 100 fs after optical excitation and ultimately determine the bandwidth of terahertz spintronic devices.

D. This paper

Here, we use terahertz emission spectroscopy to reliably measure UDM and TST in one setup. Our data reveal that the rate of UDM in F samples [Fig. 1(a)] and the rate of TST in $F|N$ stacks [Fig. 1(b)] have identical time evolution.

The measurements along with an analytical model based on Boltzmann-type rate equations and the Stoner approach to ferromagnetism show that UDM and TST are driven by a common dominant force: a generalized spin voltage of the electrons in F, which scales with the instantaneous excess magnetization. In contrast, Seebeck-type contributions due to optically induced temperature gradients and interfacial OISTR are found to make a minor contribution to the terahertz signal.

Importantly, both spin voltage and electron temperature can be defined for arbitrary, nonthermal electron distributions, which often prevail in experiments with femtosecond laser pulses.

These insights open interesting perspectives and synergies because they allow us to better understand and ultimately optimize TST by exploiting the extensive knowledge about UDM. For example, our results indicate that the temporal onset of TST is only determined by the duration of the femtosecond pump pulse. They suggest that the amplitude of TST can, in principle, be increased by one order of magnitude.

II. EXPERIMENTAL SETUP

A. Samples and excitation

As F materials, we choose the metallic ferromagnets $Co_{70}Fe_{30}$ (CoFe), $Co_{40}Fe_{40}B_{20}$ (CoFeB), and $Ni_{80}Fe_{20}$ (NiFe), whose metallic components are predominantly ferromagnetic transition metals. We choose NiFe since it has a significantly larger electron-spin relaxation time than CoFeB and CoFe [71].

For N, we choose the spin-to-charge-current conversion materials Pt and W because they exhibit large yet opposite spin Hall conductivities [34]. Two thin films of F and $F|N$ are grown by magnetron sputtering on the same diamond substrate, which is transparent at all relevant terahertz and optical frequencies. The sample preparation is detailed in Appendix A 1.

The direction of the sample magnetization $\mathbf{M}$ is set by an external magnetic field of ∼10 mT either parallel or antiparallel to the y-axis unit vector $\mathbf{u}_y$ [Fig. 1(a)]. The sample under investigation is excited with linearly polarized laser pulses (wavelength of 800 nm, duration of ∼10 fs, and pulse energy of 2 nJ) from a Ti : sapphire laser oscillator (repetition rate of 80 MHz) under normal incidence. The pump beam diameter at the sample position is ∼25 μm full width at half maximum of the intensity.

The total thickness of the metal stack is significantly smaller than the penetration depth of the pump field (∼30 nm). As a consequence and as confirmed by calculations, the pump field is constant throughout the thickness of the metal film to very good approximation (Fig. S1 [72]).

B. Measurement of UDM and TST

1. Terahertz field emission

To measure the dynamics of the magnetization $\mathbf{M}(t) = M(t)\mathbf{u}_y$ of an F sample [Fig. 1(a)] and of the spin current flowing from F into an adjacent N [Fig. 1(b)] vs time t, the concomitantly emitted terahertz electromagnetic pulse is used as a probe. UDM [Fig. 1(a)] implies a dynamic magnetic dipole that generates an electromagnetic pulse [73–76] with an electric field

$$E_M(t) \propto d_F \partial_t M(t), \tag{1}$$

directly behind the sample (see Appendix A 2). Here, $\partial_t = \partial/\partial t$ denotes the time derivative, and d_F is the thickness of F.

In TST [Fig. 1(b)], the spin-current density $\mathbf{j}_s(t) = j_s(t)\mathbf{u}_z$ across the $F|N$ interface is instantaneously converted [77] into a transverse charge-current density proportional to $j_s(t)$ by the inverse spin Hall effect in N. It results in a time-dependent electric dipole and, thus, emission of an electromagnetic pulse with transient electric field [34–37]

$$E_{j_s}(t) \propto j_s(t), \tag{2}$$

behind the sample (see Appendix A 2). As the dynamics are driven by a femtosecond laser pulse, the bandwidths of E_M and E_{j_s} are expected to extend to frequencies well >10 THz.

In our setup, we detect any transient electric field $E(t)$ such as $E_{j_s}(t)$ and $E_M(t)$ by electro-optic sampling [78–81], where a probe pulse (0.6 nJ, 10 fs) copropagates with the terahertz pulse through an electro-optic crystal. The ellipticity $S(t)$ accumulated by the sampling pulse is measured as a function of the delay t between terahertz and sampling pulse by means of a polarization-sensitive optical bridge, which consists of a quarter-wave plate, a polarizing beam splitter, and two balanced photodiodes. As an electro-optic crystal, we use GaP(110) (thickness of 250 μm) or ZnTe(110) (1 mm or 10 μm). All experiments are performed at room temperature in a dry N_2 atmosphere.

2. From signals to fields

To focus on magnetic effects, we only consider the signal component odd in the sample magnetization:

$$S(t) = \frac{S(t, \mathbf{M}) - S(t, -\mathbf{M})}{2}. \tag{3}$$

The waveform $S(t)$ is related to the terahertz electric field $E(t)$ directly behind the sample by the convolution [82]

$$S(t) = (H_{SE} * E)(t) = \int d\tau \, H_{SE}(t-\tau)E(\tau). \tag{4}$$

The transfer function $H_{SE}(t)$ connects S and E and accounts for the terahertz pulse propagation to the detection and the electro-optic sampling process [52,74,82]. We determine H_{SE} by using a well-understood reference emitter, GaP(110), with a thickness of 50 μm [82]. To numerically solve Eq. (4) for $E(t)$, the convolution is time discretized and recast in the form of a matrix equation [82]. From $E(t)$, we straightforwardly obtain $\partial_t M(t)$ [Eq. (1)] and $j_s(t)$ [Eq. (2)] with an estimated time resolution of 40 fs (see Sec. III D).

3. Expected signal contributions

The total terahertz field behind the $F|N$ stacks with N = Pt or W is dominated by E_{j_s} [34]. Due to its electric-dipole character, $E_{j_s}(t)$ fully reverses when the $F|N$ stack is turned by 180° about an axis parallel to $\mathbf{M}$ [Fig. 1(b)]. In contrast, the field E_M from the F sample originates from magnetic dipoles. It, thus, remains invariant under 180° sample

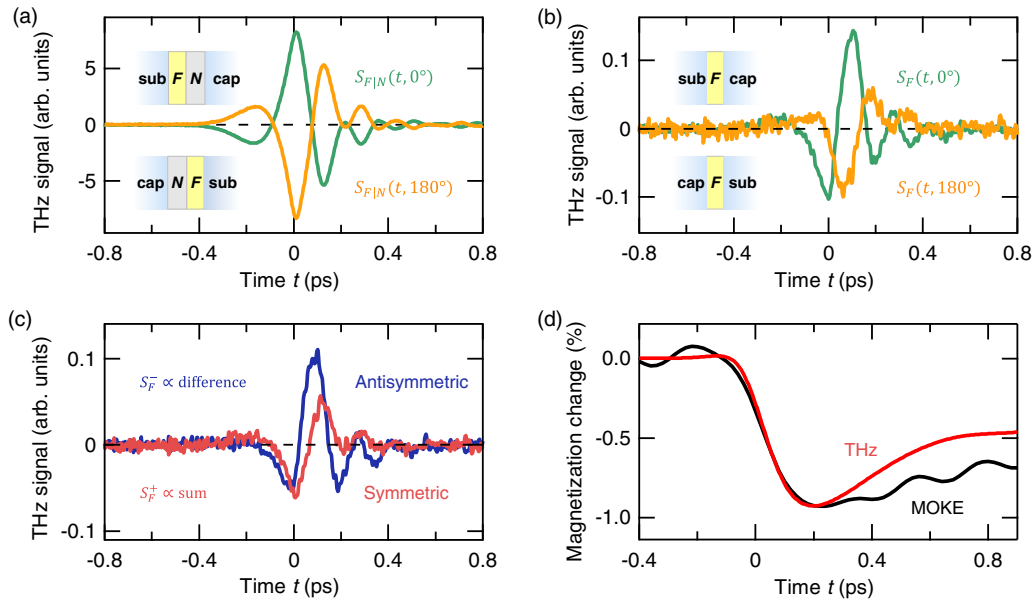

FIG. 2. Typical terahertz electro-optic signals, odd with respect to magnetization **M**, from F and $F|N$ samples consisting of $F =$ CoFe(3 nm) and $N =$ Pt(3 nm). (a) Terahertz emission signal $S_{F|N}(t, 0°)$ from an $F|N$ stack. When the sample is turned by 180° about **M**, the signal $S_{F|N}(t, 180°)$ is obtained. Note that the sample is optically symmetrized by a cap window that is identical to the diamond substrate (see insets). (b) Same as (a) but for the F sample. Note the substantial asymmetry between $S_F(t, 0°)$ and $S_F(t, 180°)$. (c) Resulting signals $S_F^+(t)$ and $S_F^-(t)$ symmetric and antisymmetric with respect to sample turning. (d) Extracted magnetization dynamics from $S_F^+(t)$ of (c) (red curve), along with magnetization dynamics as measured by the magneto-optic Kerr effect (MOKE, black curve). The magnetization evolution derived from the terahertz signal was convoluted with a Gaussian (123 fs full width at half maximum) to match the time resolution of the MOKE measurement.

turning [Fig. 1(a)] [75,76] and is typically up to two orders of magnitude smaller [74] than E_{j_s}.

The small field E_M can easily be masked by spurious electric-dipole-type signals that arise when inversion symmetry is broken, either by the sample structure or by gradients of the pump intensity along the sample depth. To minimize pump-induced gradients [83], the F thickness d_F is chosen sufficiently small. To discriminate electric-dipole signals due to a possible inversion asymmetry of the F sample [84], we measure it both in the 0° and 180°-turned configuration. To achieve a symmetric configuration regarding the propagation of optical pump and terahertz pulses, the samples are macroscopically symmetrized by adding a cap layer (cap) that is identical to the substrate [sub; see inset of Fig. 2(a)].

Details of this separation procedure and two more complementary approaches are described in Appendix A 3.

4. Magneto-optic probing

For comparison with UDM probed by terahertz spectroscopy [Eq. (1)], we also conduct a pump-probe experiment, in which the pump-induced change $\Delta M(t)$ in the F-sample magnetization is interrogated by an optical probe pulse through the transient magneto-optic Kerr effect (MOKE) [13]. We measure both the MOKE-induced rotation and ellipticity of the probe-pulse polarization behind the sample, as detailed in Appendix A 4.

Note that the pump-induced MOKE signal contains contributions from $\Delta M(t)$ and changes in the magneto-optic coefficients. A separation and deconvolution procedure [13] allows us to extract $\Delta M(t)$ from the MOKE trace with a time resolution of 130 fs, provided the pump-pulse energy has not yet been transferred from the electrons into the phonons of F. At later pump-probe delays (typically >0.3 ps), the increased phonon temperature leads to additional signal contributions unrelated to $\Delta M(t)$ [13].

III. RESULTS

A. Terahertz emission signals

Figures 2(a) and 2(b) display typical terahertz electro-optic signals $S_{F|N}(t)$ and $S_F(t)$ from, respectively, $F|N$ and F samples with $F =$ CoFe(3 nm) and $N =$ Pt(3 nm). According to Eq. (3), all waveforms are odd with respect to the magnetization **M**. The signal components even in **M** are >40 times smaller (Fig. S2 [72]). The polarization of the terahertz pulses associated with $S_{F|N}(t)$ and $S_F(t)$ is linear with the electric field perpendicular to **M** (Fig. S3 [72]), consistent with the emission scenarios of Fig. 1.

1. F|N sample

Figure 2(a) shows the signal $S_{F|N}(t, \theta = 0°)$ from the sub||$F|N$||cap sample. As expected from Fig. 1(b), it is antisymmetric with respect to turning the sample and, thus, reverses completely in the 180°-configuration cap||$F|N$||sub: $S_{F|N}(t, \theta = 0°) = -S_{F|N}(t, \theta = 180°)$. We note that we use this antisymmetric behavior to turn the sample around with

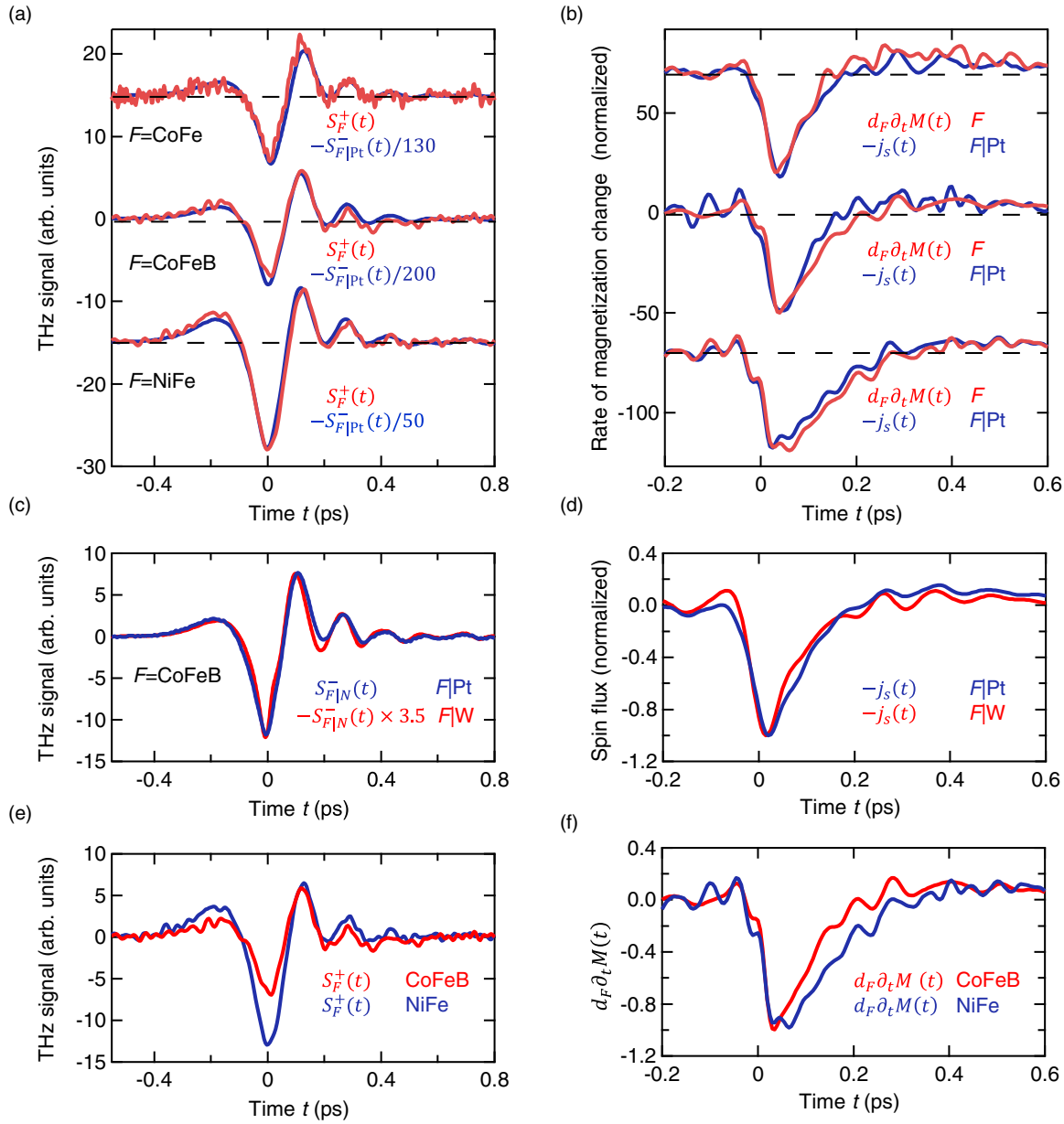

FIG. 3. Terahertz emission due to terahertz spin transport (TST) in $F|N$ stacks vs ultrafast demagnetization (UDM) in F samples. (a) Terahertz signal $S_{F|N}^-(t)$ from an $F|N$ stack with $F =$ CoFe(3 nm) and $N =$ Pt(3 nm), antisymmetric with respect to sample turning about **M** (blue solid line), vs terahertz signal $S_F^+(t)$ from a single F layer, symmetric with respect to sample turning (red solid line). The curves below show analogous signals for F and $F|N$ samples with $F =$ CoFeB(5 nm) and $F =$ NiFe(9 nm). Curves are scaled by the indicated factors and offset vertically for clarity. (b) Temporal evolution of the spin current $j_s(t)$ flowing in the $F|N$ sample and of the rate of change $\partial_t M(t)$ of the magnetization of the F sample times the F thickness d_F, as extracted from the data of (a). Curves are vertically offset and normalized to their minima to allow for a better comparison of the relaxation dynamics. (c) Direct comparison of the signals $S_{F|N}^-(t)$ from the stacks $F|$Pt(3 nm) and $F|$W(3 nm) with $F =$ CoFeB(3 nm) and (d) the resulting spin current dynamics. (e) Direct comparison of the signals $S_F^+(t)$ from single $F =$ CoFeB(3 nm) (red) and NiFe(3 nm) (blue) films and (f) the resulting rate of magnetization change.

high precision (see Appendix A 3). Very similar signals are observed for W as for the N material [Fig. 3].

2. *F sample*

The terahertz signals from the F sample [Fig. 2(b)] are two orders of magnitude smaller than from the $F|N$ counterpart. When the sample is turned, the signal does not fully invert but changes its shape. This behavior indicates a superposition of contributions being symmetric (+) and asymmetric (−) under sample turning. To separate them, we calculate the signals

$$S_F^{\pm}(t) = \frac{S_F(t, \theta = 0^\circ) \pm S_F(t, \theta = 180^\circ)}{2}, \tag{5}$$

which are displayed in Fig. 2(c). We emphasize that we can consistently and reliably reproduce $S_F^+(t)$ using two more complementary approaches, as detailed in Appendix A 3, Supplemental Note 1, and Figs. S4–S8 [72].

The magnitude of the asymmetric component S_F^- is comparable with that of S_F^+. This observation suggests that the F sample exhibits noticeable inversion asymmetry. It is not unexpected because thin films are known to exhibit inhomogeneities along the growth direction and to possess different properties at the substrate interface as compared with the bulk [85].

The symmetric component $S_F^+(t)$ contains the contribution E_M due to UDM [Fig. 1(a)]. Assuming that S_F^+ solely arises from E_M, we retrieve $E_M(t)$ and, thus, the evolution of the magnetization change $\Delta M(t)$ (see Sec. II B). To compare $\Delta M(t)$ with the transient MOKE signals (Sec. II B), we match the lower time resolution of the MOKE waveform by convoluting $\Delta M(t)$ with a Gaussian of 123 fs full width at half maximum. The accordingly filtered $\Delta M(t)$ from the terahertz measurements is shown in Fig. 2(d) (red curve) along with the magnetization dynamics measured by the transient MOKE (black curve).

The initial quenching dynamics of the two signals agree fully. However, for times $t > 0.3$ ps, $\Delta M(t)$ evolves somewhat more slowly for the MOKE-based signal than for the terahertz-derived dynamics. We ascribe this moderate discrepancy to MOKE-signal contributions that are unrelated to magnetization dynamics and instead arise from pump-induced heating of the crystal lattice [13]. We conclude that the sign, magnitude, and shape of the terahertz-emission-derived $\Delta M(t)$ is fully consistent with the notion that the signal $S_F^+(t)$ arises from UDM of the F sample as given by Eq. (1).

B. UDM vs TST

We can now directly compare the terahertz signal waveforms $S_F^+(t)$ due to UDM of a single layer of $F =$ CoFe [Fig. 1(a)] with waveforms $S_{F|N}^-(t)$ due to TST from F into $N =$ Pt [Fig. 1(b)]. The result is shown in Fig. 3(a) and reveals a remarkable correlation: The terahertz signals $S_F^+(t)$ and $S_{F|N}^-(t)$ exhibit identical dynamics: $S_{F|N}^-(t) \propto S_F^+(t)$.

We emphasize that we make analogous observations for two other ferromagnets $F =$ CoFeB and NiFe [Fig. 3(a)] as well as for W as N material [Fig. 3(c)]. Interestingly, as seen in Fig. 3(e), the terahertz emission signals $S_F^+(t)$ for $F =$ CoFeB (dashed black line) and NiFe (blue solid line) have a significantly different shape: While the global minimum and maximum of the signals for $F =$ CoFeB have approximately the same magnitude, the magnitude of the minimum signal for $F =$ NiFe is a factor of $\sim$2 larger than the magnitude of the maximum. These drastic differences are also observed in the spectra of the signals (Fig. S9(b) [72]) and the resulting magnetization evolution $M(t)$ (Fig. S9(d) [72]). They indicate significantly different dynamics for the two ferromagnets CoFeB and NiFe.

Strikingly, however, the agreement of the dynamics of $S_F^+(t)$ and $S_{F|N}^-(t)$ for each of the F materials remains [Fig. 3(a)]. These observations are confirmed for different thicknesses of $F =$ CoFeB and NiFe (Fig. S10 [72]) and for an electro-optic terahertz detector with enhanced sensitivity at frequencies >20 THz (Fig. S11 [72]).

Our observation $S_{F|N}^-(t) \propto S_F^+(t)$ and the origins of $S_{F|N}^-$ [Eq. (1)] and S_F^+ [Eq. (2)] imply that

$$j_s(t) \propto \partial_t M(t). \tag{6}$$

In other words, our terahertz emission signals directly show that, on ultrafast timescales, the photoinduced spin current in an $F|N$ stack has a temporal evolution that is identical to that of the rate of photoinduced magnetization quenching of an F sample.

The most explicit manifestation of Eq. (6) is Fig. 3(b), which shows the dynamics of j_s and $\partial_t M$ as retrieved from the signals $S_{F|N}^-$ and S_F^+ (see Sec. II B). As expected from the terahertz signals $S_F^+(t)$ and $S_{F|N}^-(t)$, both $j_s(t)$ and $\partial_t M(t)$ evolve quite differently for the samples with $F =$ CoFeB and NiFe. They decay markedly slower for NiFe than for CoFeB.

Equation (6) summarizes our central experimental result. We stress that $j_s(t)$ and $\partial_t M(t)$ refer to very different samples $F|N$ vs F. Consequently, Eq. (6) does not arise from the trivial fact that transport from F to N reduces the F magnetization at the same rate. In our experiment, the rate $\partial_t M(t)$ is measured for a simple F sample, in which spin transport out of F is disabled. Therefore, the identical dynamics of $\partial_t M(t)$ and $j_s(t)$ reveals a profound relationship between UDM of an F sample [Fig. 1(a)] and TST in an $F|N$ stack [Fig. 1(b)].

C. Driving force

1. Relevant mechanisms

As summarized in Sec. I B, TST as observed here can arise from bandlike transport, shiftlike transport (OISTR), and inverse spin-orbit torque. The latter is typically two orders of magnitude smaller than the remaining contributions [63]. In addition, in our experiment, the pump pulses are linearly (not circularly) polarized, and we do not find a terahertz field component parallel to the sample magnetization (Fig. S3 [72]). Therefore, inverse spin-orbit torque is negligible here.

Likewise, we can safely exclude that OISTR makes a significant contribution to the terahertz emission signal from the $F|N$ stacks studied here. First, OISTR should have a relaxation length of less than a unit-cell width in N (0.4 nm in Pt), which is significantly smaller than measured spin-current relaxation lengths [35,40] (1.2 nm [40]). Second, while OISTR should not be effective through intermediate layers, experiments report a sizeable spin-current decay length of several nanometers [40] in a Cu intermediate layer [36,40]. Third, for OISTR, the spin-current density $j_s(t)$ should rise and fall like the intensity envelope of the pump pulse. In contrast, the initial peak of the measured $j_s(t)$ is much wider [100–130 fs full width at half maximum, Fig. 3(b)] than our time resolution ($\sim$40 fs).

We, thus, conclude that the TST observed here is dominated by bandlike transport.

2. Model

To better understand the connections between UDM and TST, we develop a simple microscopic model of these processes. To this end, we follow Ref. [18] and treat the electronic structure and the ferromagnetism of F in the framework of the Stoner model [86,87] and describe the dynamics with Boltzmann-type rate equations [88]. Accordingly, the

schematic of Fig. 4(a) displays the density of states of spin-up (↑) and spin-down (↓) electrons vs single-electron energy ϵ.

We assume that UDM primarily arises from quasi-elastic spin flips [10] [white arrow in Fig. 4(a)] and that the pump pulse can be considered a small perturbation of the system. At a given ϵ, the probability of a spin-flip event is proportional to the difference $n^{F\uparrow}(\epsilon,t) - n^{F\downarrow}(\epsilon,t)$, where $n^{F\sigma}(\epsilon,t) = n_0(\epsilon) + \Delta n^{F\sigma}(\epsilon,t)$ denotes the occupation number of a Bloch state with spin σ (↑ or ↓) and energy ϵ in F. It is a sum of the distribution n_0 of the unexcited sample and the pump-induced changes $\Delta n^{F\sigma}$. The rate $\partial_t M(t)$ of magnetization change is obtained by integrating over all energies ϵ.

Similarly, the spin current $j_s(t)$ from F to N in the $F|N$ stack is inferred by counting all spin transmission events across the $F|N$ interface [Fig. 4(b)]. As detailed in the Appendix B, we find that

$$\left.\begin{matrix}\partial_t M(t)\\ j_s(t)\end{matrix}\right\} \propto \Delta\tilde{\mu}_s(t) + (\text{Seebeck contribution}), \tag{7}$$

where the quantity

$$\Delta\tilde{\mu}_s(t) = \int d\epsilon\ (n^{F\uparrow} - n^{F\downarrow})(\epsilon,t) \tag{8}$$

has the same form for $\partial_t M(t)$ and $j_s(t)$, whereas the Seebeck contribution differs. Remarkably, Eq. (7) is fully consistent with our central experimental finding [Eq. (6)] if $\Delta\tilde{\mu}_s$ dominates. Consequently, we consider $\Delta\tilde{\mu}_s$ and the Seebeck terms in more detail.

3. Spin voltage

If the occupation numbers $n^{F\sigma}$ in Eq. (8) are Fermi-Dirac functions with chemical potentials $\mu^{F\sigma}$, $\Delta\tilde{\mu}_s$ equals the spin voltage [61,64] $\mu^{F\uparrow} - \mu^{F\downarrow}$ indicated in Figs. 4(a) and 4(b). Therefore, $\Delta\tilde{\mu}_s$ can be considered a generalized spin voltage that is caused by an electron distribution with an arbitrary, possibly nonthermal imbalance $\Delta n^{F\uparrow} - \Delta n^{F\downarrow}$. Upon absorption of the pump pulse, $\Delta\tilde{\mu}_s$ rises immediately because spin-up and spin-down electrons in a Stoner-type ferromagnet possess a very different electronic density of states around the Fermi level [see Fig. 4(a)].

4. Impact of temperature gradients

The Seebeck-type term [64] in Eq. (7) is proportional to the difference $\Delta\tilde{T}^{F\uparrow} - \Delta\tilde{T}^{F\downarrow}$ in the case of $\partial_t M(t)$ [Eq. (B17)], whereas it equals a linear combination of $\Delta\tilde{T}^{F\uparrow} - \Delta\tilde{T}^{N\uparrow}$ and $\Delta\tilde{T}^{F\downarrow} - \Delta\tilde{T}^{N\downarrow}$ for $j_s(t)$ [Eq. (B18)]. Here, $\Delta\tilde{T}^{X\sigma}$ is the pump-induced change in the generalized temperature of electrons with spin σ in $X = F$ or N. It scales with the electronic excess energy [Eqs. (B35) and (B37)] and equals the conventional temperature change once the electron distribution is thermal.

To estimate the $F|N$ peak temperature differences $\Delta\tilde{T}_0^{F\sigma} - \Delta\tilde{T}_0^{N\sigma}$ directly after excitation by the pump pulse, we assume the same temperature for spin-up and spin-down electrons and an incident fluence of 0.1 mJ/cm^2. For CoFeB(3 nm)|Pt(3 nm), we obtain $\Delta\tilde{T}_0^{F\sigma} - \Delta\tilde{T}_0^{N\sigma} = 160$ K. This value is sizeable because it is comparable with the temperature increase $\Delta\tilde{T}_0^{F\sigma} = 200$ K of F.

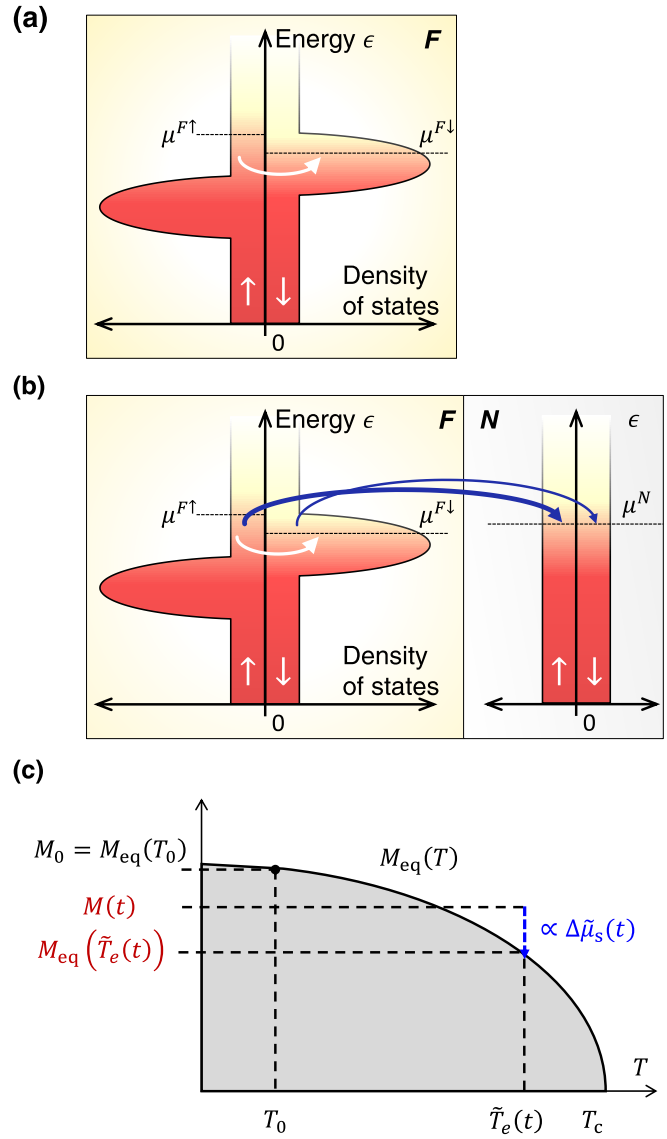

FIG. 4. Simple model of ultrafast demagnetization (UDM) and terahertz spin transport (TST). (a) UDM. Schematic of the density of states of spin-up (↑) and spin-down (↓) Bloch electrons of a metallic ferromagnet such as Fe in the framework of the Stoner model. Quasi-elastic spin-flip scattering events (white curved arrow) lead to transfer of spin angular momentum to the crystal lattice. (b) TST. N acts as an additional sink of spin angular momentum through spin-conserving electron transfer across the $F|N$ interface (blue curved arrows). In (a) and (b), the spin transfer rate scales with the generalized spin voltage $\Delta\tilde{\mu}_s$ [Eq. (7)], which equals $\mu^{F\uparrow} - \mu^{F\downarrow}$ in the case of Fermi-Dirac electron distributions. (c) Illustration of the interplay of spin voltage, electron temperature, and magnetization according to Eq. (9). At time $t = 0$, the pump pulse excites the sample with temperature T_0, causing a time-dependent uniform increase of the generalized electronic temperature to $\tilde{T}_e(t) = T_0 + \Delta\tilde{T}_e(t)$ (dashed line). At any subsequent time $t > 0$, the system aims to change its magnetization from the instantaneous value $M(t)$ to $M_{eq}[\tilde{T}_e(t)]$, where $M_{eq}(T)$ is the equilibrium magnetization vs temperature T (black solid line). The spin voltage $\Delta\tilde{\mu}_s(t)$ is proportional to the excess magnetization $M(t) - M_{eq}[\tilde{T}_e(t)]$ [blue dashed arrow, see Eq. (9)]. Note that this consideration is strictly valid only in the small-perturbation regime where $M(t) \approx M_0$ (see Appendix B 7).

To evaluate the impact of the initial $F|N$ temperature difference on spin transport, we note that the Seebeck contribution to $\partial_t M(t)$ and $j_s(t)$ in Eq. (7) is a linear combination of very different terms: $\Delta\tilde{T}^{F\uparrow} - \Delta\tilde{T}^{F\downarrow}$ vs $\Delta\tilde{T}^{F\uparrow} - \Delta\tilde{T}^{N\uparrow}$ and $\Delta\tilde{T}^{F\downarrow} - \Delta\tilde{T}^{N\downarrow}$. Therefore, the Seebeck component would result in different dynamics of $\partial_t M(t)$ and $j_s(t)$ if it was significant. However, as we observe identical dynamics [Figs. 3(a) and 3(b)], the Seebeck terms very likely play a minor role in our photoexcited F and $F|N$ samples.

To check this conclusion further, we compare the spin-current dynamics in CoFeB(3 nm)|Pt(3 nm) to that in CoFeB(3 nm)|W(3 nm), the latter of which exhibits ~4 times larger electronic temperature difference $\Delta\tilde{T}_0^{F\sigma} - \Delta\tilde{T}_0^{N\sigma} = 608$ K directly after pump excitation. If a Seebeck contribution was relevant, one should observe different spin-current dynamics in the two samples. Again, however, we observe almost identical dynamics [Figs. 3(c) and 3(d)]. Therefore, TST and UDM in our samples are predominantly driven by a transient spin voltage rather than temperature gradients.

According to Eqs. (B17) and (B18), two reasons can explain the negligible Seebeck contribution in our data. (i) The Seebeck coefficients are small, and/or (ii) the electronic temperature differences $\Delta\tilde{T}^{F\uparrow} - \Delta\tilde{T}^{F\downarrow}$ and $\Delta\tilde{T}^{F\sigma} - \Delta\tilde{T}^{N\sigma}$ relax faster than our time resolution of 40 fs. We consider it unlikely that reason (i) applies universally to the manifold of samples studied here. In contrast, scenario (ii) is very plausible because energy transport can be very efficient directly after optical excitation. During this early stage, a large fraction of the excited electrons is found at energies of up to $\hbar\omega_p = 1.6$ eV above the Fermi level, where $\hbar\omega_p$ is the pump photon energy. Each of these electrons carries up to 2 orders of magnitude more energy than a thermal electron relative to the Fermi level [82]. Consequently, energy equilibration between F and N is expected to be much faster than spin equilibration by spin transport, where constantly $\hbar/2$ of spin angular momentum is transferred per electron, independent of the electron energy.

To summarize, our experiments strongly indicate that temperature differences between spin-up and spin-down electrons and electrons in F and N make a minor contribution to UDM and TST. This behavior likely arises because all electronic subsystems $X\sigma$ attain approximately equal generalized temperatures faster than our time resolution of 40 fs. Consequently, we consider only one common generalized electron temperature $\Delta\tilde{T}^{X\sigma} = \Delta\tilde{T}_e$ in the following.

5. Dominant driving force

Our observations [summarized by Eq. (6)] and modeling [leading to Eq. (7)] directly imply that the generalized spin voltage $\Delta\tilde{\mu}_s$ of F is the dominant driving force of both UDM [Fig. 1(a)] and TST [Fig. 1(b)]. Therefore, the traces of $\partial_t M(t)$ and $j_s(t)$ in Fig. 3(b) directly monitor the evolution $\Delta\tilde{\mu}_s(t)$ of the spin voltage. Notably, the dynamics for CoFeB and CoFeB|Pt agree well with a spin-voltage transient of Fe on W that was measured by time-resolved photoelectron emission spectroscopy recently [61].

We expect the spin voltage to be larger when the magnetization of F is further away from its instantaneous equilibrium value. Indeed, our modeling in Appendix B shows that, in the limit of uniform electron temperature and small transient magnetization changes [$M(t) \approx M_0$], the generalized spin voltage scales according to

$$\Delta\tilde{\mu}_s(t) \propto M(t) - M_{\mathrm{eq}}[\tilde{T}_e(t)]. \tag{9}$$

In other words, $\Delta\tilde{\mu}_s(t)$ is proportional to the transient excess spin density, that is, the difference between the instantaneous magnetization $M(t)$ and the equilibrium magnetization $M_{\mathrm{eq}}[\tilde{T}_e(t)]$ that would be attained at the instantaneous generalized electron temperature $\tilde{T}_e(t) = T_0 + \Delta\tilde{T}_e(t)$. This remarkable and highly intuitive theoretical result is illustrated by Fig. 4(c).

D. Modeling the spin dynamics

To understand the shape of the temporal evolution of $\Delta\tilde{\mu}_s$ and, thus, $\partial_t M(t)$ in the F sample and j_s in the $F|N$ stack, we remark that $\Delta\tilde{\mu}_s$ and the uniform generalized electron excess temperature $\Delta\tilde{T}_e$ are connected by Eqs. (7) and (9). As shown in Appendix B, one obtains

$$\Delta\tilde{\mu}_s(t) \propto \Delta\tilde{T}_e(t) - \Gamma_{\mathrm{es}} \int_0^\infty d\tau\, \exp(-\Gamma_{\mathrm{es}}\tau)\, \Delta\tilde{T}_e(t-\tau), \tag{10}$$

where $\Gamma_{\mathrm{es}}^{-1}$ is the time constant of electron-spin equilibration. To illustrate Eq. (10), we consider a steplike increase of the generalized uniform electron temperature. Once $\Delta\tilde{T}_e$ jumps to a nonzero value, $\Delta\tilde{\mu}_s$ follows without delay according to the first term on the right-hand side of Eq. (10). It triggers transfer of spin angular momentum from the F electrons into the F lattice (UDM) and possibly into N (TST). The loss of excess magnetization, however, decreases $\Delta\tilde{\mu}_s$ through Eq. (9). Consequently, $\Delta\tilde{\mu}_s$ decays on the timescale $\Gamma_{\mathrm{es}}^{-1}$, as dictated by the second term of Eq. (10).

In our experiment, the excess energy of the F electrons and, thus, $\Delta\tilde{T}_e$ rise instantaneously upon pump-pulse excitation, and they subsequently decay due to energy transfer to the crystal lattice [88,89]. As shown in Appendix C, we can accordingly model the evolution of $\Delta\tilde{T}_e$ by

$$\Delta\tilde{T}_e(t) \propto \Theta(t)[(1-R)\exp(-\Gamma_{\mathrm{ep}}t) + R], \tag{11}$$

where $\Theta(t)$ is the Heaviside step function, $\Gamma_{\mathrm{ep}}^{-1}$ is the time constant of electron-phonon equilibration, and R is the ratio of electronic and total heat capacity of the sample. With these assumptions, Eqs. (7) and (10) yield the simple result

$$\left.\begin{matrix}\partial_t M(t) \\ j_s(t)\end{matrix}\right\} \propto \Theta(t)[A_{\mathrm{es}}\exp(-\Gamma_{\mathrm{es}}t) - A_{\mathrm{ep}}\exp(-\Gamma_{\mathrm{ep}}t)], \tag{12}$$

where $A_{\mathrm{es}} = (\Gamma_{\mathrm{es}} - R\Gamma_{\mathrm{ep}})/(\Gamma_{\mathrm{es}} - \Gamma_{\mathrm{ep}})$ and $A_{\mathrm{ep}} = (1-R)\Gamma_{\mathrm{ep}}/(\Gamma_{\mathrm{es}} - \Gamma_{\mathrm{ep}})$.

We apply Eq. (12) to our measured data in Fig. 5 in two steps. First, to account for the experimental time resolution, Eq. (12) is convoluted with a Gaussian of 40 fs full width at half maximum, which matches the initial rise time of the calculated and all measured $\partial_t M(t)$ and $j_s(t)$. Second, we take only Γ_{es} and the rather trivial overall amplitude as free sample-dependent fit parameters. For Γ_{ep} and R, literature values are assumed (see Appendix C and Table S2 [72]).

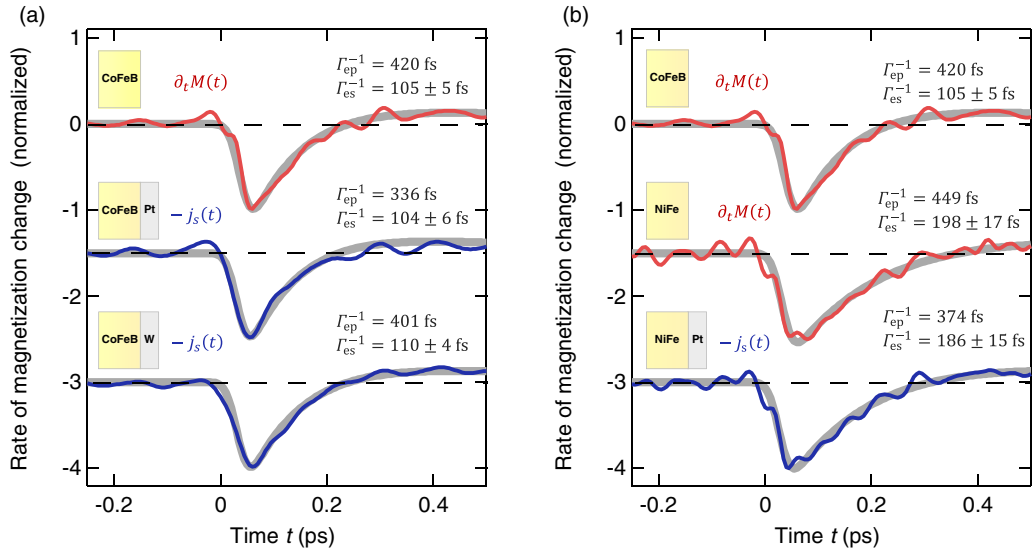

FIG. 5. Measured and modeled dynamics of the rate of magnetization change $\partial_t M(t)$ in F samples and the spin-current density $j_s(t)$ from F to N in $F|N$ stacks. (a) Evolution of $\partial_t M(t)$ of an F = CoFeB sample (red solid line) and $j_s(t)$ in $F|$Pt and $F|$W stacks (blue solid lines). Gray solid lines are fits based on Eq. (12) with Γ_{es} and the overall amplitude scaling as the only fit parameters. (b) Analogous to (a) but for $\partial_t M(t)$ in CoFeB and $j_s(t)$ in NiFe and NiFe|Pt.

Figure 5 demonstrates that Eq. (12) excellently describes the experimentally determined $\partial_t M(t)$ and $j_s(t)$.

IV. DISCUSSION

Our experiments show that UDM of an F sample and TST in an $F|N$ stack exhibit identical temporal dynamics [Fig. 3 and Eq. (6)]. Combination of this observation with our model [Eq. (7)] implies that UDM and TST are predominantly driven by the spin voltage $\Delta\tilde{\mu}_s(t)$ rather than temperature gradients. The modeling also very well captures the temporal dynamics of $\partial_t M(t)$ and $j_s(t)$ by only three parameters: Γ_{es}, Γ_{ep}, and R [Fig. 5 and Eq. (12)]. In the following, we discuss the impact of N and F materials on the dynamics of $\Delta\tilde{\mu}_s(t)$ and potential extensions of our model.

A. Impact of N and F on dynamics

1. Impact of N

At first glance, Fig. 1 suggests that the presence of N modifies the dynamics of the spin voltage in F due to (i) additional spin relaxation, which increases Γ_{es}, and (ii) different overall cooling dynamics of the electrons, which alters Γ_{ep}. However, the identical temporal evolution of $\Delta\tilde{\mu}_s$ in the F and $F|N$ samples [Figs. 3(b) and 3(d)] shows that the coupling to N does not significantly perturb the dynamics of (i) spins and (ii) electrons in F.

To discuss this behavior quantitatively, we consider Eq. (12) and note that the slope of the curves $\partial_t M(t)$ and $-j_s(t)$, normalized to the respective minimum, approximately equals $-(\Gamma_{es}+\Gamma_{ep})$ right after excitation (Fig. 5). The reason is that both electron-spin (Γ_{es}) and electron-phonon (Γ_{ep}) equilibration contribute to the decay dynamics of $\Delta\tilde{\mu}_s$. For an F sample with F = CoFeB, we find Γ_{es}^{-1} = 104 fs [Fig. 5(a)], which agrees with previous reports [90] and is four times smaller than Γ_{ep}^{-1} = 420 fs. Therefore, we have $\Gamma_{es} \gg \Gamma_{ep}$, and the slope of the initial decay of $\partial_t M(t)$ is dominated by Γ_{es}.

When N = Pt is attached to CoFeB, we expect a larger Γ_{es} (due to the new spin dissipation channel of TST) and an increase of Γ_{ep} by 20% (see Table S2 [72]). In contrast, we experimentally observe an equally fast decay of $\partial_t M(t)$ and $j_s(t)$ [Fig. 5(a)], as confirmed by our fits, which yield a very similar Γ_{es}^{-1} for CoFeB and CoFeB|Pt. Therefore, the time constant Γ_{es}^{-1} of F and $F|N$ samples is almost the same. In other words, TST into the Pt layer surprisingly does not accelerate spin-electron equilibration (Γ_{es}) in CoFeB, and the slightly faster electron cooling (Γ_{ep}) is negligible because $\Gamma_{ep} \ll \Gamma_{es}$. This finding is further supported by the nearly identical spin-current dynamics $j_s(t)$ in CoFeB|W and CoFeB|Pt [Figs. 3(d) and 5(a)]. We, thus, reveal a large potential for increasing the amplitude of TST, which, in our samples, has only a minor impact on electron-spin equilibration.

2. Impact of F material

We finally test NiFe as an F material because its Γ_{es} is known to be substantially smaller than for CoFeB [71]. Indeed, both $\partial_t M(t)$ and $j_s(t)$ decay 50% more slowly for NiFe ($\Gamma_{es}^{-1} \approx 200$ fs) than for CoFeB ($\Gamma_{es}^{-1} \approx 100$ fs) [Figs. 3(f) and 5(b)]. This observation is consistent with previous work [71] in which a slower electron-spin relaxation for NiFe (demagnetization time of 190 fs) than for Fe (demagnetization time of 100 fs) was reported. In contrast, Γ_{es} remains the same for the NiFe|Pt and NiFe samples within our experimental uncertainty.

B. Model implications

Our experimental results and the model developed here have important implications regarding the magnitude of the spin current and its relaxation time.

1. Fluence dependence

First, we emphasize that Eq. (9) and, thus, Fig. 4(c) are even valid for large excitation fluences, provided one considers small times $t_0 \ll 1/\Gamma_{es}$ directly after optical sample excitation, that is, when the magnetization is still unchanged [$M(t_0) \approx M_0$, see Appendix B 10]. According to Eq. (9) and Fig. 4(c), an increase of the pump fluence and, thus, the peak electron temperature $\tilde{T}_e(t_0)$ should result in a monotonically increasing spin-current amplitude $j_s(t_0)$. However, once $\tilde{T}_e(t_0)$ exceeds the Curie temperature T_C, an abrupt saturation of $j_s(t_0)$ and, thus, the emitted terahertz peak field should occur. These expectations were recently confirmed in a terahertz emission study, in which the pump fluence was varied over a large range [47].

2. Temperature dependence

According to our model, the time constant Γ_{es}^{-1} is proportional to the magnetic spin susceptibility χ^F of the F material [Eq. (B33)]. Because χ^F increases with the equilibrium temperature T_0 up to the Curie temperature T_C [Eq. (B23)], our model implies a slowing down of UDM and TST as T_0 increases. For UDM, this notion is consistent with previous experiments [12] and simulations [18]. For TST, it is the subject of ongoing experiments.

The preceding considerations are certainly qualitative but nevertheless demonstrate the predictive power of our model.

C. Possible model extensions

Our analytical model of UDM and TST successfully describes all experimental observations of this paper and makes predictions about the fluence and temperature dependence of UDM and TST, which are consistent with previous studies. It even applies to nonthermal electron distributions, which are ubiquitous in the first 100 fs following optical excitation of metals [82].

The central ingredients of our model are the Stoner approach to the electronic structure, rate equations, and quasi-elastic electron scattering to describe the dynamics of the Bloch states and the linearization of energy-dependent coefficients around the Fermi energy. A uniform electronic temperature in the vicinity of the $F|N$ interface followed from a comparison of experiment and theory, as addressed in Sec. III C. In the following, we discuss the soundness of other relevant model assumptions and possible extensions if other material systems or observables are of interest.

1. The Stoner model as phenomenological model

The Stoner model is presumably the simplest approach to ferromagnetism in a single-electron framework [86]. It includes the exchange interaction between electrons through an effective magnetic field that is proportional to the mean local spin polarization. Therefore, the Stoner model captures magnons only through their mean impact on the spin polarization but neglects the transverse spin fluctuations they induce.

Despite these restrictions, the Stoner model is routinely used to successfully explain magnetoresistive phenomena such as tunneling and giant magnetoresisctance [87] and spin-caloritronic effects such as the spin-dependent Seebeck and anomalous Nernst effects [64,91]. The Stoner model was also successfully used for numerical simulations of UDM of $3d$-type metallic ferromagnets [18] and to fit instantaneous photoelectron emission spectra of optically excited Co [92]. In the latter case, however, partially unrealistic values of the Stoner model fit parameters emerged. We conclude that the Stoner model provides a good phenomenological description of various magnetism phenomena, but the values of the microscopic parameters should not be overinterpreted.

Consequently, in our treatment (Appendix B 7), all microscopic Stoner-model parameters are eventually replaced by macroscopic observables such as the temperature-dependent equilibrium magnetization M_{eq} and the magnetic spin susceptibility χ^F.

2. Beyond the Stoner model

An extended description of our experiment could make use of an sd-type model, in which localized magnetic moments and their transverse fluctuations are described by a Heisenberg Hamiltonian for d-type electrons, whereas bandlike spin transport arises from s-like electrons [19–21].

Recently, sd-type descriptions of UDM [19–21] and TST [20,21] were established. They should enable a better understanding of the role of magnons and possibly allow one to calculate more complex observables such as photoelectron emission spectra [30,55]. A future task is to extend the sd-type approach to more complex magnets such as ferrimagnets [93] and to nonthermal electron [13] and magnon [94] distributions.

3. Electron scattering and moment expansion

So far, we model electron scattering without spin conservation as quasi-elastic single-electron processes. Therefore, electron-electron collisions that do not conserve the total electron spin are neglected. They could be included with a more elaborate treatment [18], which is not implemented here for the sake of simplicity. Spin-conserving electron-electron scattering is, however, fully accounted for.

Our model assumes that microscopic quantities such as the electronic density of states [Fig. 4(c)] can be linearized around the Fermi energy. As detailed in Ref. [13], this assumption is justified because, only 30 fs after optical excitation, the transient electron distribution is most likely significantly <1 eV wide. On this energy scale, the calculated densities of states of Fe, Co, and Ni vary roughly linearly [95]. Note that a possible Stoner gap in the single-electron excitation spectrum is not relevant in our model. The considered spin-flip processes arise from electron-impurity and electron-phonon scattering and, thus, do not constrain the scattering phase space due to conservation of the electron wave vector.

4. Crystal lattice dynamics

Each electronic spin-flip event in our model implies transfer of angular momentum to the crystal lattice. One could further resolve this transfer with respect to phonon wave vector and frequency by suitable rate equations for the crystal-lattice degrees of freedom. Such an extension could be interesting for the description of diffraction experiments resolving ultrafast motion of the crystal lattice [15,16].

5. Spin voltage in N

Our model neglects a possible spin voltage in N throughout the considered time interval. This assumption is justified for Pt because its spin relaxation time of 15 fs [96] is shorter than all other timescales in our experiment. However, for N materials with longer spin relaxation time, a sizeable spin accumulation can be expected that hampers and possibly slows down the spin transfer from F to N. This expectation is consistent with numerical simulations of spin transport in Fe|Ru stacks, which indicated a significant spin accumulation in the Ru regions close to the Fe/Ru interface along with slower spin-transport dynamics [28]. Such a feedback effect could be straightforwardly included in our model by allowing for a nonvanishing spin voltage in the N layer.

To summarize, the preceding discussion shows that the assumptions of our modeling are justified and that its scope in terms of materials and observables can be extended even further by moderate extensions.

D. Conclusions

Our experiments and analysis based on a simple model of UDM and TST allow us to draw significant conclusions from both a fundamental and applied viewpoint.

1. Spin voltage vs temperature gradient

UDM and TST are driven by the same force: a generalized spin voltage [Eq. (7)], which quantifies the excess of spin polarization relative to the current equilibrium value [see Fig. 4(c) and Eq. (9)]. We suggest to term the heat-induced spin voltage the pyrospintronic effect because it is analogous to the pyroelectric effect of a pyroelectric material, in which the spontaneous electric polarization is forced to follow the instantaneous temperature. The pyrospintronic effect is a predominantly ultrafast effect because the relaxation time of the spin voltage is limited by the electron-spin relaxation time, which typically amounts to 100 fs and less in typical metallic ferromagnets.

We emphasize that our measured spin current is not the result of a spin-dependent Seebeck effect [64]: To quantitatively explain our data, we must assume neither a temperature difference between F and N nor between majority and minority electrons in F. It appears that temperature gradients become relevant (i) on longer timescales, when the spin voltage has decayed, or (ii) in structures where F is not excited, implying no change in spin voltage. An example of (i) is the spin-dependent Seebeck effect under stationary conditions [97–99]. An example of (ii) is an $F|$Pt stack with an insulating F material such as yttrium iron garnet [82,100], which is not excited when the photon energy of the pump pulse is smaller than the electronic bandgap.

2. Spin-voltage decay

After the pump pulse has excited the electronic system of F, the generalized spin voltage and, thus, $\partial_t M(t)$ and $j_s(t)$ jump to a nonzero value and subsequently relax by electron-spin equilibration, while the significantly slower electron-phonon equilibration has a minor influence. Our results strongly suggest that the impact of TST on Γ_{es} is negligible in our experiments.

The previous conclusion implies that the photoinduced spin voltage primarily decays due to spin-flip processes in F also in the $F|N$ stack. In other words, only a small fraction of the available excess spin angular momentum is transferred to N. We, thus, anticipate that the spin-current amplitude can, in principle, be increased significantly by using more transparent $F|N$ interfaces [101] and F materials with larger electron-spin relaxation time Γ_{es}^{-1}.

3. Peak current and bandwidth

Regarding speed and bandwidth, we note that the temporal onset of TST is truly ultrafast and predominantly only limited by the duration of the pump-pulse depositing energy in the electrons of F [see Eq. (10) and Fig. 5]. This feature is in remarkable contrast to the interfacial spin-Seebeck effect [82], where carrier multiplication is required to reach maximum spin current.

To optimize the peak amplitude and relaxation time of the spin current in metallic $F|N$ stacks, Appendix B 10 provides relationships of these characteristics to microscopic and macroscopic material quantities.

4. Impact on other research fields

Importantly, our study allows us to apply the extensive knowledge about UDM of F samples to TST from F to an adjacent layer N. This insight is expected to be very helpful to boost spin-current amplitudes in numerous applications such as spin torque [31,33], spintronic terahertz emitters [34–37], and potentially energy harvesting [102]. Our findings also provide a straightforward link between concepts of femtomagnetism and spintronics. Terahertz emission spectroscopy holds great promise to be an excellent ultrafast monitor of the evolution of the generalized spin voltage.

ACKNOWLEDGMENTS

We thank Dr. Yuta Sasaki for contributions in an early stage of this paper and Dr. Daniela Zahn for helpful discussions. We acknowledge funding by the German Research Foundation through the collaborative research center SFB TRR 227 "Ultrafast spin dynamics" (project ID 328545488, projects A05, B01, B02, and B03) and the priority program SPP 1666 "Topological Insulators" and funding by the European Union through the ERC H2020 CoG project TERAMAG/grant no. 681917. We also acknowledge support by the International Max Planck Research School for Elementary Processes in Physical Chemistry.

APPENDIX A. EXPERIMENTAL DETAILS

1. Sample preparation and characterization

The F samples (where F is $Co_{60}Fe_{20}B$, $Co_{70}Fe_{30}$, or $Ni_{80}Fe_{20}$) and $F|N$ stacks (where N is Pt or W) are grown by means of magnetron sputtering. The deposition is performed at an Ar pressure of 4×10^{-3} mbar at growth rates between 0.2 and 1 Å/s, depending on the material. Half of the substrate is covered by a metallic mask during deposition of the N

material, thereby resulting in an F sample and an $F|N$ stack on the same substrate and in the same run. All samples are protected by a 10-nm-thick Al_2O_3 layer grown by atomic layer deposition. As substrates, we choose diamond and, for test purposes, fused silica.

Magnetic hysteresis loops show that the samples have a coercive field <10 mT. We also measure the optical absorptance A of the pump pulse and the sample impedance Z from 1 to 7 THz, as detailed in Ref. [62]. We find that Z is approximately independent of frequency. Values of A, Z, and the mean terahertz conductivity are compiled in Table S3 [72].

2. Signals due to TST and UDM

For the $F|N$ stack, the signal is dominated by TST and the inverse spin Hall effect in N, which converts the electron spin current with density $(\hbar/2)j_s$ into a charge current with density $(-e)j_c$. Here, $\hbar$ is the Planck constant, $-e$ is the electron charge, and $j_c = \theta_{\mathrm{SH}} j_s$ with θ_{SH} being the spin Hall angle of the N material. In the frequency domain, the terahertz electric field behind the sample is related to the spin current injected into the Pt layer by a generalized Ohm's law [34]:

$$E_{j_s}(\omega) = eZ(\omega)\theta_{\mathrm{SH}}(\omega)\lambda_{\mathrm{rel}} j_s(\omega). \tag{A1}$$

Terahertz transmission measurements and broadband measurements of the anomalous Hall effect of magnetic metals [77] show that the sample impedance $Z(\omega)$ and the spin Hall angle $\theta_{\mathrm{SH}}(\omega)$ are constant over the relevant frequency range and for the diamond substrates used here. Therefore, Eq. (A1) yields $E_{j_s}(t) \propto j_s(t)$ in the time domain.

Using eqs. (2) and (5) of Ref. [75], we find that the time-dependent magnetization of the F sample gives rise to magnetic-dipole radiation with an electric field

$$E_M(\omega) = -\frac{i\omega n(\omega) d_F}{c} Z(\omega) M(\omega), \tag{A2}$$

directly behind the sample. Here, $n(\omega)$ is the refractive index of the half-space (substrate or cap window) facing away from the terahertz detection, d_F is the F thickness, and c is the speed of light. Equation (A2) can also be obtained from eq. (S3) in Ref. [28] by expanding the phase factors up to first order in the argument and by subsequently considering that the refractive index of the metal film is much larger than $n(\omega)$ at terahertz frequencies. Finally, as the $n(\omega)$ of diamond and the sample impedance $Z(\omega)$ are approximately constant for all relevant frequencies $\omega/2\pi$, Eq. (A2) leads to $E_M(t) \propto \partial_t M(t)$ in the time domain.

3. Measurement configurations

a. Symmetry considerations

The terahertz emission signal from the $F|$Pt and $F|$W samples is dominated by the electric-dipole field E_{j_s} [Fig. 1(b)]. In contrast, the terahertz magnetic-dipole field E_M from the F sample [Fig. 1(a)] is typically two orders of magnitude smaller. It can easily be masked by spurious electric-dipole-type signals that arise when inversion symmetry is broken, either by the sample structure [structural inversion asymmetry (SIA)] or by the perturbing light field [light-induced inversion asymmetry (LIA)]. For example, SIA can be caused by inequivalent interfaces of F [84], and LIA can arise from a change of the pump intensity across the F thickness [83].

To discriminate a terahertz electric-dipole field E_{SIA} due to SIA from E_M, three different approaches are implemented. In the first approach, we symmetrize the sample by adding a cap layer (cap) that is identical to the substrate [sub; see inset of Fig. 2(b)]. We measure the sample both in the 0° configuration sub$||F||$cap and the 180°-turned configuration cap$||F||$sub. While E_{SIA} changes sign [62], E_M stays invariant.

To minimize the field E_{LIA} owing to LIA, which is also invariant under sample turning, we choose an F thickness much thinner than the attenuation length of the optical pump field ($\sim$30 nm). Calculations show that, in our metal stacks, the pump field changes by $<5\%$ over the full thickness of up to 10 nm (Fig. S1 [72]).

b. Implementation

We acquire terahertz emission data from the F sample and the associated $F|N$ stack, both of which are grown on the same substrate and can be reached by translating the sample perpendicularly to the pump beam. As sample spots, we choose F and $F|N$ regions as close as possible to guarantee identical optical environments for the probed F and $F|N$ thin film regions. To reproducibly put the metal film into the focal region of the pump spot, we use crossed beams of alignment lasers to mark the position and tilt angle of the sample. To test for correct alignment, we check that the emission signals from the 0° and 180° sample configurations of the $F|N$ sample are reversed versions of each other.

In the second approach, we measure unsymmetrized samples sub$||F$ and sub$||F|N$ analogous to the first method. Because of its macroscopic asymmetry, the signals from the 0° and 180° configurations of the sub$||F|N$ sample are in general not reversed versions of each other anymore. The two signals are, however, connected by a transfer function that can easily be inferred and, in turn, applied to the two signals from the sub$||F$ sample. More details and a third separation method working in reflection mode are presented in Supplemental Note 1 and Figs. S4–S8 [72]. We emphasize that all three separation methods deliver highly consistent results.

4. Magneto-optic probing of magnetization dynamics

To interrogate the magnetization dynamics of the F sample by the MOKE, we conduct a pump-probe measurement [13] in which pump and probe pulses are incident onto the sample under 50° angle of incidence. Pump pulses (duration of 200 fs, center wavelength of 400 nm, and repetition rate of 1 kHz) are obtained by frequency doubling of pulses from a Ti : sapphire laser amplifier. Probe pulses (40 fs, 800 nm, and 80 MHz) are taken from the seed oscillator of the amplifier [94]. During reflection off the sample, the probe polarization acquires an additional rotation and ellipticity, part of which is proportional to the sample magnetization averaged over the probing volume [13].

The pump-induced polarization variation of the reflected probe pulse is measured using a balanced detection scheme. In our samples, rotation and ellipticity signals have the same dynamics, indicating negligible pump-induced variation of magneto-optic coefficients [13]. We confirm that the response

is linear with respect to the used pump fluence of up to 1 mJ/cm^2. To push the time resolution down to 130 fs, the pump-probe transient is deconvoluted with the pump-pulse profile.

APPENDIX B. SPIN-DYNAMICS MODEL

Our goal is to model the spin dynamics of a single thin ferromagnetic metal layer F and an $F|N$ stack where F is in contact with a thin normal metal layer N. We assume that each layer X (F or N) can be treated as homogeneous.

1. Electronic structure

We describe the electronic structure of F and N by the Stoner model [86] in which a given electron feels the exchange coupling to other electrons through the mean magnetization $\mathbf{M} = M\mathbf{u}_y$ (Fig. 1). Transverse spin fluctuations perpendicular to $\mathbf{M}$ due to magnons are summarized by the reduced magnitude of $\mathbf{M}$. The Stoner model provides a good phenomenological description of various magnetism phenomena [18,64,87,91,92], but its microscopic parameters should not be overinterpreted [92].

The state of the electronic system in a given layer X is fully characterized by the occupation numbers $n_k^{X\sigma}$ of a Bloch state (k,σ). Here, $\sigma = \uparrow, \downarrow$ refers to the electron spin, and k summarizes the band index and wave vector. We define the magnetic moment $\mathbf{m} = m\mathbf{u}_y$ of F such that $(g^F/2)\mu_B m = MV^F$, where $g^F \approx 2$ is the electron g factor, μ_B is the Bohr magneton, and V^F is the volume of F. Similarly, we define the spin current through the interface as $J_s = j_s A^{F|N}$, where $(\hbar/2)j_s$ is the spin-current density, and $A^{F|N}$ is the area of the $F|N$ stack.

We adopt a simplified description in which the occupation of each Bloch state (k,σ) is fully given by its energy $\epsilon_k^\sigma(t)$, that is,

$$n_k^{X\sigma}(t) = n^{X\sigma}\left[\epsilon_k^{X\sigma}(t), t\right]. \tag{B1}$$

To model magnetic order, we make use of the Stoner model, in which the Bloch energy depends on the pump-induced change Δm in the magnetic moment according to

$$\epsilon_k^{X\sigma}(t) = \epsilon_{k0}^{X\sigma} + I^{X\sigma}\Delta m(t) + e\Phi^X(t). \tag{B2}$$

Here, $\epsilon_{k0}^{X\sigma}$ is the Bloch energy before arrival of the pump pulse, and $I^{X\sigma} = I^{X\uparrow,\downarrow} = \pm I^X/2$ quantifies the strength of the effective electron-electron Coulomb interaction for $X = F$ only. The electrostatic potential Φ^X accounts for a possible charging of a given layer X due to transport, where $-e$ is the electron charge.

2. Rate equations

Before arrival of the pump pulse, $n^{X\sigma}(\epsilon,t)$ are given by one and the same Fermi-Dirac function $n_0(\epsilon)$ at temperature T_0. We now focus on the rate of change $\dot{n}^{F\sigma} = \partial_t n^{F\sigma} = \partial n^{F\sigma}/\partial t$ of the electron occupation numbers $n^{F\sigma}$ in F. As detailed in the following, it is determined by four contributions:

$$\dot{n}^{F\sigma} = \dot{n}^{F\sigma}|_{\rm sc} + \dot{n}^{F\sigma}|_{\rm sf} + \dot{n}^{F\sigma}|_{\rm tr} + \dot{n}^{F\sigma}|_I. \tag{B3}$$

The first term on the right-hand side of Eq. (B3) captures spin-conserving (sc) scattering events and the excitation by the pump pulse. It, thus, fulfills

$$0 = \int d\epsilon\, D^{F\sigma}\dot{n}^{F\sigma}|_{\rm sc}, \tag{B4}$$

where $D^{X\sigma}(\epsilon,t) = \sum_k \delta[\epsilon - \epsilon_k^{X\sigma}(t)]$ is the instantaneous density of Bloch states with spin σ.

Impurity- or phonon-mediated spin-flip (sf) events are captured by the second term of Eq. (B3) and assumed to be quasi-elastic following Refs. [10,67]. They are not restricted to so-called Stoner excitations, in which the electron wave vector is conserved [86]. As indicated by Fig. 4(a), the rate of change of the electron occupation $n^{F\uparrow}$ due to elastic spin-flip scattering is proportional to $n^{F\uparrow}$ and the number $(1-n^{F\downarrow})D^{F\downarrow}$ of available unoccupied spin-down states at the same energy ϵ plus an analogous term for the reverse process:

$$\begin{aligned}\dot{n}^{F\uparrow}|_{\rm sf} &= -P_{\rm sf}^F n^{F\uparrow}(1-n^{F\downarrow})D^{F\downarrow} + P_{\rm sf}^F n^{F\downarrow}D^{F\downarrow}(1-n^{F\uparrow}) \\ &= -(n^{F\uparrow} - n^{F\downarrow})\frac{g_{\rm sf}}{D^{F\uparrow}}.\end{aligned} \tag{B5}$$

Here, $g_{\rm sf}(\epsilon) = (P_{\rm sf}^F D^{F\uparrow}D^{F\downarrow})(\epsilon)$, and the factor $P_{\rm sf}(\epsilon)$ is proportional to the square of the matrix element for a spin-flip scattering event. The analogous equation for the rate of change of $n^\downarrow(\epsilon)$ is obtained by simply swapping $\uparrow$ and $\downarrow$.

The third term of Eq. (B3) captures spin transport (tr) across the $F|N$ interface [see Fig. 4(b)]. We assume the transmission events to be spin-conserving and elastic. Consequently, we can consider spin-up ($\sigma = \uparrow$) and spin-down ($\sigma = \downarrow$) electrons separately. By counting transmission events analogous to Eq. (B5), we obtain

$$\dot{n}^{F\sigma}|_{\rm tr} = -(n^{F\sigma} - n^{N\sigma})\frac{g_{\rm tr}^\sigma}{D^{F\sigma}}, \tag{B6}$$

where $g_{\rm tr}^\sigma(\epsilon) = (T_{\rm tr}^\sigma D^{F\sigma}D^{N\sigma})(\epsilon)$, and $T_{\rm tr}^\sigma(\epsilon)$ is a spin-dependent interface transmittance.

The last term of Eq. (B3) arises because n is evaluated at a fixed ϵ while the Bloch energy changes according to Eq. (B2). We obtain

$$\dot{n}^{F\sigma}|_I = n^{F\sigma\prime}I^{F\sigma}\dot{m} = I^{F\sigma}(\partial_\epsilon n^{F\sigma})(\dot{m}|_{\rm sf} + \dot{m}|_{\rm tr}), \tag{B7}$$

where $n^{F\sigma'} = \partial_\epsilon n^{F\sigma} = \partial n^{F\sigma}/\partial\epsilon$. In the last step of Eq. (B7), we split the rate of change of the magnetization into the contributions of spin flips and spin transport. As the electronic band structure depends on the magnetic moment m [see Eq. (B2)], $D^{F\sigma}(\epsilon)$, $g_{\rm sf}(\epsilon)$, and $g_{\rm tr}^\sigma(\epsilon)$ are also time dependent. This time dependence is left implicit in our discussion.

3. Spin transfer rates

We are interested in the dynamics of the F magnetic moment

$$m = \int d\epsilon\, (D^{F\uparrow}n^{F\uparrow} - D^{F\downarrow}n^{F\downarrow}). \tag{B8}$$

Using Eq. (B5), its rate of change due to spin-flip events is given by

$$\dot{m}|_{\rm sf} = -2\int d\epsilon\, (n^{F\uparrow} - n^{F\downarrow})g_{\rm sf}^F. \tag{B9}$$

Using Eq. (B6), the spin-resolved electron current through the $F|N$ interface can be calculated by

$$J^\sigma = \int d\epsilon\ (n^{F\sigma} - n^{N\sigma}) g_{\rm tr}^\sigma. \tag{B10}$$

We note that Eqs. (B9) and (B10) yield zero spin transfer before the pump pulse arrives because, in this case, all distribution functions $n^{F\sigma}$ and $n^{N\sigma}$ equal the same Fermi-Dirac distribution n_0 with chemical potential μ_0 and temperature T_0.

4. Moment expansion

As the relevant observables $\dot{m}|_{\rm sf}$ and J^σ involve differences of distribution functions only, we focus our discussion on the difference

$$\Delta n^{X\sigma} = n^{X\sigma} - n_0, \tag{B11}$$

of the distribution function $n^{X\sigma}(\epsilon, t)$ and the equilibrium distribution n_0. We assume that $\Delta n^{X\sigma}$ is significantly nonzero only in a relatively narrow energy window around the chemical potential μ_0 of the unperturbed system and that the energy-dependent weight factors $D^{F\sigma}(\epsilon)$, $g_{\rm sf}(\epsilon)$, and $g_{\rm tr}^\sigma(\epsilon)$ can be well approximated by the Sommerfeld approximation [13]

$$W(\epsilon) \approx W(\mu_0) + W'(\mu_0)(\epsilon - \mu_0), \tag{B12}$$

where W stands for $D^{F\sigma}$, $g_{\rm sf}$, or $g_{\rm tr}^\sigma$. Integrals involving these functions, such as Eqs. (B9) and (B10), then turn into

$$\int d\epsilon\ W(\epsilon)\Delta n^{X\sigma}(\epsilon) = W(\mu_0)\Delta P^{X\sigma} + W'(\mu_0)\Delta A^{X\sigma}, \tag{B13}$$

which is just a linear combination of the zeroth and first moment of Δn^σ, that is,

$$\Delta P^{X\sigma} = \int d\epsilon\ \Delta n^{X\sigma} \quad \text{and} \quad \Delta A^{X\sigma} = \int d\epsilon\ (\epsilon - \mu_0)\Delta n^{X\sigma}. \tag{B14}$$

In the case that $n^{X\sigma} = n_0 + \Delta n^{X\sigma}$ is a Fermi-Dirac distribution with chemical potential $\mu^{X\sigma}$ and temperature $T^{X\sigma}$, the $\Delta P^{X\sigma}$ and $\Delta A^{X\sigma}$ become Fermi-Dirac integrals and reduce to

$$\Delta P^{X\sigma} = \mu^{X\sigma} - \mu_0 \quad \text{and}$$
$$\Delta A^{X\sigma} = \frac{\pi^2 k_{\rm B}^2}{6}\left[(T^{X\sigma})^2 - T_0^2\right] + \frac{1}{2}(\mu^{X\sigma} - \mu_0)^2. \tag{B15}$$

Because $(\mu^{X\sigma} - \mu_0)^2$ is typically small, one can interpret ΔP^σ and ΔA^σ, respectively, as changes in a generalized chemical potential and a squared generalized temperature. We emphasize, however, that the definitions of the moments $\Delta P^{X\sigma}$ and $\Delta A^{X\sigma}$ [Eq. (B14)] also apply to nonthermal electron distributions $n_0 + \Delta n^{X\sigma}$.

In Ref. [61], the difference $\Delta\mu_s = \Delta\mu^{F\uparrow} - \Delta\mu^{F\downarrow}$ is termed spin voltage. We accordingly term

$$\Delta P_s = \Delta P^{F\uparrow} - \Delta P^{F\downarrow} \tag{B16}$$

generalized spin voltage. In the main text, $\Delta P_{\rm s}$ is written as $\Delta\tilde{\mu}_{\rm s}$, and further below [Eq. (B35)], we will express $\Delta A^{X\sigma}$ by the generalized excess temperature $\Delta\tilde{T}^{X\sigma}$ of the $X\sigma$ electrons.

As the pump-induced variation of the electron distribution functions $n^{X\sigma}$ and, thus, the transient state of the electronic system are fully characterized by the moments $\Delta P^{X\sigma}$ and $\Delta A^{X\sigma}$, it is sufficient to determine the dynamics of $\Delta P^{X\sigma}$ and $\Delta A^{X\sigma}$. This conclusion is consistent with a recent thermodynamic treatment of ultrafast spin dynamics [68]. In the following, we will connect the phenomenological coupling coefficients of Ref. [68] with the parameters of our simplified microscopic description.

5. Relevant observables

We apply Eq. (B13) to the rate of change of the magnetic moment [Eq. (B9)]. We find

$$\dot{m}|_{\rm sf} = -2g_{\rm sf}(\mu_0)\Delta P_s - 2g'_{\rm sf}(\mu_0)(\Delta A^{F\uparrow} - \Delta A^{F\downarrow}), \tag{B17}$$

where the first term on the right-hand side describes magnetization relaxation driven by the generalized spin voltage [Eq. (B16)]. The term proportional to $\Delta A^{F\uparrow} - \Delta A^{F\downarrow}$ is a term analogous to the Seebeck effect, which contributes if the generalized temperatures of spin-up and spin-down electrons are different.

The magnetic moment of F is also modified by spin transport through the $F|N$ interface: $-\dot{m}|_{\rm tr} = J_s = J^\uparrow - J^\downarrow$. We assume vanishing charge transport $J^\uparrow + J^\downarrow = 0$ and the same chemical potential for spin-up and spin-down electrons in N, $\Delta P^{N\uparrow} = \Delta P^{N\downarrow} = \Delta P^N$. These assumptions allow us to eliminate $\Phi^N - \Phi^F$ (see Supplemental Note 2 [72]). Along with Eqs. (B10), (B13), and (B14), we find

$$\begin{aligned} -\dot{m}|_{\rm tr} &= J_s \\ &= g_{\rm tr}(\mu_0)\Delta P_s + s_{\rm tr}^\uparrow(\mu_0)(\Delta A^{F\uparrow} - \Delta A^{N\uparrow}) \\ &\quad - s_{\rm tr}^\downarrow(\mu_0)(\Delta A^{F\downarrow} - \Delta A^{N\downarrow}), \end{aligned} \tag{B18}$$

where $2g_{\rm tr}^{-1} = (g_{\rm tr}^\uparrow)^{-1} + (g_{\rm tr}^\downarrow)^{-1}$ and $s_{\rm tr}^\sigma = g_{\rm tr} g_{\rm tr}^{\sigma\prime}/g_{\rm tr}^\sigma$. The two final terms in Eq. (B18) are again of Seebeck type and vanish once the temperatures of F and N have equilibrated. In this regime, the driving force of both $\dot{m}^F|_{\rm sf}$ and $\dot{m}^F|_{\rm tr}$ is given solely by the spin voltage ΔP_s of F.

The total energy of the F electrons in the Stoner model, including their spins, is given by

$$E^F = \sum_\sigma \int d\epsilon\ (\epsilon - \mu_0) D^{F\sigma} n^{F\sigma} + \frac{1}{4} I^F m^2. \tag{B19}$$

By using $\dot{D}^{F\sigma}(\epsilon) = D^{F\sigma\prime}(\epsilon) I^{F\sigma} \dot{m}$ and Eq. (B8), we find that the rate of change obeys

$$\dot{E}^F = \sum_\sigma \int d\epsilon\ (\epsilon - \mu_0) D^{F\sigma} (\dot{n}^{F\sigma} - \dot{n}^{F\sigma}|_I), \tag{B20}$$

where the term $\dot{n}^{F\sigma}|_I$ [Eq. (B7)] considers the time-dependence of the Bloch energies.

6. Time evolution of ΔP_s

To determine the dynamics of the system and, thus, the magnetization, it is sufficient to determine the dynamics of the moments, that is, the generalized spin voltage ΔP_s and temperatures $\Delta A^{X\sigma}$. According to Eqs. (B3) and (B7), we need to consider contributions of spin flips, spin transport, and spin-conserving processes:

$$\Delta\dot{P}_s = \Delta\dot{P}_s|_{\rm sf} + \Delta\dot{P}_s|_{\rm tr} + \Delta\dot{P}_s|_{\rm sc}. \tag{B21}$$

By taking the time derivative of Eq. (B14), considering Eqs. (B5) and (B7), performing the moment expansion of Eq. (B13), and using Eq. (B17), we obtain (see Supplemental Note 2 [72])

$$\Delta\dot{P}_s|_{\mathrm{sf}} = -\frac{2}{\chi^F(\mu_0)}[g_{\mathrm{sf}}(\mu_0)\Delta P_s + s_{\mathrm{sf}}(\mu_0)(\Delta A^{F\uparrow} - \Delta A^{F\downarrow})]. \tag{B22}$$

Here,

$$\frac{1}{\chi^F(\mu_0)} = \frac{1}{2}\left(\frac{1}{D^{F\uparrow}} + \frac{1}{D^{F\downarrow}}\right)(\mu_0) - I^F \tag{B23}$$

is the inverse of the Pauli susceptibility $\chi^F = \partial m/\partial\mu_s$ of F, which depends on the electron distribution and, thus, time only implicitly through the sample magnetization m, i.e., $\chi^F(\mu_0, t) = \chi^F[\mu_0, m(t)]$. The reason is that m fully determines the variations of $D^{F\uparrow}$ and $D^{F\downarrow}$. The coefficient $s_{\mathrm{sf}} = {g_{\mathrm{sf}}}' - \chi^F g_{\mathrm{sf}}[D^{F\uparrow\prime}/(D^{F\uparrow})^2 + D^{F\downarrow\prime}/(D^{F\downarrow})^2]/2$ quantifies the Seebeck-type response of the spin voltage to a temperature difference between majority and minority electrons.

To determine the contribution of spin transport, we take the time derivative of Eq. (B14), consider Eqs. (B6) and (B7), perform the moment expansion of Eq. (B13), and use Eq. (B18). Making the same assumptions as in the derivation of Eq. (B18), we obtain

$$\Delta\dot{P}_s|_{\mathrm{tr}} = -\frac{1}{\chi^F(\mu_0)}[g_{\mathrm{tr}}(\mu_0)\Delta P_s + \tilde{s}_{\mathrm{tr}}^{\uparrow}(\mu_0)(\Delta A^{F\uparrow} - \Delta A^{N\uparrow}) - \tilde{s}_{\mathrm{tr}}^{\downarrow}(\mu_0)(\Delta A^{F\downarrow} - \Delta A^{N\downarrow})], \tag{B24}$$

where $\tilde{s}_{\mathrm{tr}}^{\sigma} = s_{\mathrm{tr}}^{\sigma} - {g_{\mathrm{tr}}^{\sigma}}'\chi^F/D^{F\sigma}$ (see Supplemental Note 2 [72]).

Excitation by the pump pulse and subsequent spin-conserving electron-electron and electron-lattice interactions also affect the occupation numbers $n^{X\sigma}$. By applying the moment expansion of Eq. (B13) to Eq. (B4), we find that spin-conserving scattering processes couple the spin voltage and the generalized temperature through

$$\Delta\dot{P}_s|_{\mathrm{sc}} = -\frac{D^{F\uparrow\prime}}{D^{F\uparrow}}(\mu_0)\Delta\dot{A}^{F\uparrow}|_{\mathrm{sc}} + \frac{D^{F\downarrow\prime}}{D^{F\downarrow}}(\mu_0)\Delta\dot{A}^{F\downarrow}|_{\mathrm{sc}}. \tag{B25}$$

Equation (B21), along with Eqs. (B22), (B24), and (B25), determines the dynamics of the spin voltage, provided the dynamics of the squared generalized temperatures $\Delta A^{X\sigma}$ are given. In these equations, the prefactors of $\Delta A^{X\sigma}$ and ΔP_s depend on the instantaneous state of the system and, thus, on the time-dependent occupation numbers $n^{X\sigma} = n_0 + \Delta n^{X\sigma}$.

7. Example: Uniform electron temperature

It is instructive to summarize the preceding considerations for the example of a uniform electron temperature ΔA. This situation is realized in our experiments because no indication of Seebeck-type contributions is observed. Therefore, the total rate of change in the magnetic moment of F can be written as

$$\dot{m} = -g_{\mathrm{tot}}(\mu_0)\Delta P_s, \tag{B26}$$

where $g_{\mathrm{tot}} = 2g_{\mathrm{sf}} + g_{\mathrm{tr}}$ summarizes the contribution of spin flips [Eq. (B17)] and spin transport [Eq. (B18)].

For a uniform electron temperature, the state variables ΔP_s and ΔA fully determine the pump-induced changes in the electron distributions of F and N and, thus, in all other observables. Indeed, combination of Eqs. (B21)–(B26) yields

$$\dot{m} = a\Delta\dot{P}_s + b\Delta\dot{A}. \tag{B27}$$

The prefactors $a(t) = a[m(t)] = \chi^F(\mu_0)$ and $b(t) = b[m(t)] = \chi^F(\mu_0)(D^{F\uparrow\prime}/D^{F\uparrow} - D^{F\downarrow\prime}/D^{F\downarrow})(\mu_0)$ depend on time t only through $m(t)$ because, in the Stoner model, changes in the electronic band structure are mediated solely by m. Note that, in standard thermodynamics of a system with state variables μ_s and T, Eq. (B27) corresponds to the total differential

$$dm = \frac{\partial m}{\partial\mu_s}d\mu_s + \frac{\partial m}{\partial T}dT. \tag{B28}$$

To connect $b(m)$ in Eq. (B27) to macroscopic observables, we consider an infinitesimal quasistatic process $P_s \to P_s + dP_s$ and $A \to A + dA$. Because the system is in equilibrium at the start and end of this process, we have $dP_s = 0$. Equation (B27) leads to $dm = b\,dA$ and, thus,

$$b(m) = {m_{\mathrm{eq}}}'(A) = \chi^F(\mu_0)\left(\frac{D^{F\uparrow\prime}}{D^{F\uparrow}} - \frac{D^{F\downarrow\prime}}{D^{F\downarrow}}\right)(\mu_0), \tag{B29}$$

with $m = m_{\mathrm{eq}}(A)$. In other words, $b(m)$ equals the slope of the equilibrium magnetization curve $m_{\mathrm{eq}}(A)$. Combination of Eqs. (B27) and (B29) yields the remarkable result

$$\Delta\dot{P}_s(t) = \frac{1}{\chi^F(\mu_0)}\frac{\partial}{\partial t}\{m(t) - m_{\mathrm{eq}}[A(t)]\}. \tag{B30}$$

It shows that, in the limit of uniform electron temperature, a change in the spin voltage is directly proportional to a change in the difference between the instantaneous magnetization $m(t)$ and the equilibrium magnetization $m_{\mathrm{eq}}[A(t)]$ at the instantaneous electron temperature $A(t)$. In the limit of small magnetization changes with $m(t) \approx m_0$, the susceptibility $\chi^F(\mu_0, t) = \chi^F[\mu_0, m(t)]$ [Eq. (B23)] becomes time-independent, and Eq. (B30) turns into Eq. (9) and Fig. 4(c).

We emphasize that, in the relevant Eqs. (B17), (B18), and (B30), all microscopic Stoner model parameters, such as electronic densities of states and the Coulomb-interaction parameter, are replaced by macroscopic observables: the temperature-dependent equilibrium magnetization m_{eq}, the generalized electron temperature A, the magnetic spin susceptibility χ^F, and the coefficients g_{sf} and g_{tr}. All preceding considerations also apply to nonthermal electron distributions.

8. Linear excitation limit

From now on, we focus on the limit of weak optical excitation of the F and $F|N$ samples. In fact, in our experiments, all terahertz emission signals were found to scale linearly with the incident pump-pulse energy up to the maximum available incident fluence of 0.2 mJ/cm^2. Therefore, $\dot{m}$ and J_s and, through Eqs. (B17) and (B18), ΔP_s and $\Delta A^{X\sigma}$, and by Eq. (B14), the changes in the occupation numbers $\Delta n^{X\sigma}$ are also directly proportional to the deposited pump power. It follows that the prefactors in Eqs. (B22), (B24), and (B25) are independent of the pump-induced changes $\Delta n^{X\sigma}$ in the occupation numbers and can, thus, be evaluated for the unperturbed system. This simplification has important consequences.

a. Dynamics

First, we can solve Eq. (B21) along with Eqs. (B22), (B24), and (B25) for the spin voltage ΔP_s. We find that ΔP_s is a convolution:

$$\Delta P_s(t) = -(H_{\rm es}\,\Delta F)(t) = -\int d\tau\; H_{\rm es}(t-\tau)\Delta O(\tau), \tag{B31}$$

of a driving force ΔO with a response function

$$H_{\rm es}(t) = \Theta(t)\exp(-\Gamma_{\rm es}t), \tag{B32}$$

where $\Theta(t)$ is the Heaviside step function. The exponential decay rate equals

$$\Gamma_{\rm es} = \frac{2g_{\rm sf}+g_{\rm tr}}{\chi^F}(\mu_0), \tag{B33}$$

for the $F|N$ stack. By setting $g_{\rm tr}=0$, $\Gamma_{\rm es}$ for the F sample is obtained. The expression for the driving force ΔO is

$$\Delta O = \frac{D^{F\uparrow\prime}}{D^{F\uparrow}}\Delta\dot{A}^{F\uparrow}|_{\rm sc} - \frac{D^{F\downarrow\prime}}{D^{F\downarrow}}\Delta\dot{A}^{F\downarrow}|_{\rm sc} + \frac{s_{\rm sf}}{\chi^F}(\Delta A^{F\uparrow}-\Delta A^{F\downarrow}) + \frac{\tilde{s}^{\uparrow}_{\rm tr}}{\chi^F}(\Delta A^{F\uparrow}-\Delta A^{N\uparrow}) - \frac{\tilde{s}^{\downarrow}_{\rm tr}}{\chi^F}(\Delta A^{F\downarrow}-\Delta A^{N\downarrow}). \tag{B34}$$

Here, all prefactors should be evaluated at $\epsilon=\mu_0$ and for the unperturbed system, thereby making them time independent. The first two terms of ΔO cause a change in the spin voltage, and they scale with the time derivative of the pump-induced excess energy of spin-up and spin-down electrons. The remaining terms are Seebeck-type terms that disappear when the generalized temperatures of all electron subsystems $X\sigma$ have the same value. The last two terms in Eq. (B34) are omitted for the case of an F sample.

b. Temperature and energy

Second, the pump-induced change in the squared generalized temperature [Eq. (B15)] of electron system $X\sigma$ simplifies to

$$\Delta A^{X\sigma} = \frac{\pi^2 k_{\rm B}^2}{3}T_0\Delta\tilde{T}^{X\sigma}, \tag{B35}$$

where $T_0+\Delta\tilde{T}^{X\sigma}$ can be interpreted as generalized temperature of the $X\sigma$ electrons. The expression for the generalized chemical potential $\mu_0+\Delta P^{X\sigma}=\mu_0+\Delta\tilde{\mu}^{X\sigma}$ remains unchanged.

Third, the rate of change of the energy of the X electrons [see Eq. (B20)] simplifies to

$$\dot{E}^F = \sum_\sigma\int d\epsilon\,(\epsilon-\mu_0)D_0^{F\sigma}\dot{n}^{F\sigma} = \sum_\sigma C_e^{F\sigma}\partial_t\Delta\tilde{T}^{F\sigma}, \tag{B36}$$

where $C_e^{X\sigma}=(\pi^2k_{\rm B}^2/3)T_0D_0^{X\sigma}(\mu_0)$, and $C_e^X=C_e^{X\uparrow}+C_e^{X\downarrow}$ is the heat capacity of the X electrons. Here, we neglected terms of order $(\epsilon-\mu_0)^2$ in the spirit of the moment expansion of Eq. (B13). Therefore, the excess energy of the F electrons is

$$\Delta E^F = \sum_\sigma C_e^{X\sigma}\Delta\tilde{T}^{X\sigma}, \tag{B37}$$

which underscores the interpretation of $T_0+\Delta\tilde{T}^{X\sigma}$ as generalized temperature.

9. Dynamics for uniform electron temperature

Owing to Eqs. (B17), (B18), (B31), and (B34), the dynamics of UDM and TST are fully determined by a linear combination of $\Delta A^{X\sigma}$ and, because of Eq. (B35), the generalized excess temperatures $\Delta\tilde{T}^{X\sigma}$ of all electron subsystems $X\sigma$.

To develop a simple model for the time dependence of the generalized temperature, we briefly review the processes following photoexcitation of metal thin films [89]. At time $t=0$, the δ-like pump pulse excites the sample, thereby causing a steplike increase of the electronic excess energy and, thus, of all $\Delta\tilde{T}^{X\sigma}$.

Due to electron-electron interactions, all electronic subsystems $X\sigma$ quickly reach thermal equilibrium with each other, resulting in approximately equal generalized electronic temperatures $\Delta\tilde{T}^{X\sigma}=\Delta\tilde{T}_e$. In this limit, the Seebeck-type contributions to the magnetization dynamics [Eqs. (B17) and (B18)] and to the driving force ΔO [Eq. (B34)] are absent. Because we do not observe any signature of Seebeck-type terms in our experiment (Sec. III C), we assume one uniform electron temperature:

$$\Delta\tilde{T}^{X\sigma} = \Delta\tilde{T}_e, \tag{B38}$$

at all times.

a. Spin dynamics

As a consequence, Eqs. (B34), (B35), and (B29) turn the driving force for the spin voltage into

$$\Delta O = \frac{m'_{\rm eq}(T_0)}{\chi^F(\mu_0)}\Delta\dot{\tilde{T}}_e, \tag{B39}$$

where $\chi^F(\mu_0)$ should be evaluated for the unperturbed system. Equations (B39) and (B31) result in

$$\Delta P_s = -\frac{m'_{\rm eq}(T_0)}{\chi^F(\mu_0)}\dot{H}_{\rm es} * \Delta\tilde{T}_e, \tag{B40}$$

which is equivalent to Eq. (10). The resulting magnetization dynamics due to spin flips and transport follows from Eq. (B40) and, respectively, $\dot{m}|_{\rm sf}=-2g_{\rm sf}(\mu_0)\Delta P_s$ [Eq. (B17)] and $J_s=g_{\rm tr}(\mu_0)\Delta P_s$ [Eq. (B18)]. Integration of $\dot{m}|_{\rm sf}$ and taking advantage of $\Gamma_{\rm es}=2g_{\rm sf}/\chi^F$ yields

$$\Delta m|_{\rm sf} = m_{\rm eq}{}'(T_0)\Gamma_{\rm es}H_{\rm es} * \Delta\tilde{T}_e. \tag{B41}$$

b. Relaxation of $\Delta\tilde{T}_e(t)$

To model the dynamics $\Delta\tilde{T}_e(t)$ of the generalized electron temperature, we note that electron-electron scattering and, thus, carrier multiplication are not relevant for modifying the excess energy and, therefore, $\Delta\tilde{T}_e$ [see Eq. (B37)]. Electron-phonon interaction, on the other hand, causes heat transfer from the electrons to the crystal lattice with time constant $\Gamma_{\rm ep}^{-1}$. On a much longer timescale, which is not considered here, heat is transferred into the sample environment. Consequently, and as derived in Appendix C, we model the time dependence

of the generalized temperature by the ansatz

$$\Delta\tilde{T}_e(t) = \Theta(t)[\Delta\tilde{T}_\infty + (\Delta\tilde{T}_{e0} - \Delta\tilde{T}_\infty)\exp(-\Gamma_{\rm ep}t)]. \quad \text{(B42)}$$

Here, $\Delta\tilde{T}_{e0}$ is the increase of the uniform generalized temperature after absorption of the δ-like pump pulse and the fast equilibration between all electron subsystems $X\sigma$. The term $\Delta\tilde{T}_\infty = R\Delta\tilde{T}_{e0}$ is the generalized excess temperature at which the combined electron and lattice system equilibrate, with R being the ratio of electronic and total heat capacity.

With $\Delta\dot{\tilde{T}}_e = \Delta\tilde{T}_{e0}[\delta(t) - (1-R)\Gamma_{\rm ep}\Theta(t)\exp(-\Gamma_{\rm ep}t)]$ and Eq. (B40), one immediately finds that

$$\Delta P_s(t) = -\frac{m_{\rm eq}{}'(T_0)}{\chi^F(\mu_0)}\Delta\tilde{T}_{e0}\Theta(t)\left[\frac{\Gamma_{\rm es} - R\Gamma_{\rm ep}}{\Gamma_{\rm es} - \Gamma_{\rm ep}}\exp(-\Gamma_{\rm es}t) - \frac{(1-R)\Gamma_{\rm ep}}{\Gamma_{\rm es} - \Gamma_{\rm ep}}\exp(-\Gamma_{\rm ep}t)\right]. \quad \text{(B43)}$$

Without the Seebeck-type contributions, $\dot{m}|_{\rm sf}$ [Eq. (B17)] and $\dot{m}|_{\rm tr} = -j_s$ [Eq. (B18)] are both directly proportional to $\Delta P_s(t)$, and Eq. (B43) turns into Eq. (12). To account for the time resolution of our experiment, we convolute Eq. (B43) with a Gaussian of 40 fs full width at half maximum.

To fit our data with Eq. (B43), we obtain $\Gamma_{\rm ep}$ and R from previous works and Eqs. (C7) and (C8). Before fitting, all measured curves are shifted to the same time zero. The only fit parameters are $\Gamma_{\rm es}$ and an overall scaling factor. As seen in Fig. 5, we obtain excellent agreement with our measurements. All parameters and references are summarized in Table S1 [72].

10. Spin-current characteristics

Because of its relevance for applications, here, we estimate the major characteristics of the spin current $J_s = g_{\rm tr}(\mu_0)\Delta P_s$ [Eq. (B18)]. According to Eq. (B43), the maximum value is reached directly after excitation by the δ-like pump. In this early stage ($t = 0^+$), the magnetization is approximately unchanged [$m(t) \approx m_0$], and Eq. (B30) can be time integrated to yield

$$J_s(t = 0^+) = [m_0 - m_{\rm eq}(T_0 + \Delta\tilde{T}_{e0})]\frac{g_{\rm tr}}{\chi^F}(\mu_0). \quad \text{(B44)}$$

We emphasize that this relationship is valid beyond the linear excitation limit. On the other hand, when the optical excitation is sufficiently weak, we use Eqs. (B37) and (B38), the definition of $g_{\rm tr}(\mu_0)$, and assume $D^{F\uparrow}(\mu_0) \ll D^{F\downarrow}(\mu_0)$ to find that $J_s(0^+)$ scales according to

$$J_s(t = 0^+) \propto -m_{\rm eq}{}'(T_0)T_{\rm tr}^{\uparrow}\frac{D^{N\uparrow}D^{F\uparrow}}{\chi^F D^{F\downarrow}}(\mu_0), \quad \text{(B45)}$$

for a given amount of deposited pump-pulse energy. After attaining its maximum, ΔP_s [Eq. (B43)] and, thus, the spin current decay with the inverse time constant $\Gamma_{\rm es} + \Gamma_{\rm ep} \approx \Gamma_{\rm es}$ since electron-phonon relaxation is substantially slower than electron-spin relaxation (see Sec. IV A). Because in our experiment, the presence of N does not noticeably change the dynamics of F (see Sec. III B), Eq. (B33) becomes $\Gamma_{\rm es} \approx 2g_{\rm sf}/\chi^F$. Using the definition of $g_{\rm sf}(\mu_0)$, we obtain

$$\Gamma_{\rm es} \approx 2P_{\rm sf}\frac{D^{F\uparrow}D^{F\downarrow}}{\chi^F}(\mu_0), \quad \text{(B46)}$$

in the linear excitation regime. Equations (B44)–(B46) are potentially useful for optimizing the height $J_s(0^+)$ and width $1/\Gamma_{\rm es}$ of the ultrashort spin-current pulse $J_s(t)$ in future studies. While Eq. (B44) is given by macroscopic observables, we note that Eqs. (B45) and (B46) strongly depend on microscopic parameters of the Stoner model, which should be considered phenomenological parameters.

APPENDIX C. TWO-TEMPERATURE MODEL FOR NONTHERMAL STATES

To determine $\Gamma_{\rm ep}$ and R [see Eq. (B42)] for an F sample, we extend the standard two-temperature model [88,89] (2TM) to nonthermal electron and phonon distributions and, subsequently, to a two-layer stack $F|N$.

1. 2TM for *F*

To model the decay of the electronic excess heat in the F sample, we follow the argumentation of Sec. III C and Appendix B 9 and assume that all electron baths $X\sigma$ can be described by one common generalized excess temperature $\Delta\tilde{T}_e = \Delta\tilde{T}^{X\sigma}$.

a. Energy balance

Changes in the total electron energy of F arise from excitation by the pump laser and by energy transfer to the phonons. Using Eq. (B36), the rate of change of the electron excess energy can, thus, be written as

$$\Delta\dot{E}^F = C_e^F\Delta\dot{\tilde{T}}_e = \Delta\dot{E}^F|_{\rm ep} + \Delta\dot{E}^F|_{\rm pump}, \quad \text{(C1)}$$

where $C_e^F = C_e^{F\uparrow} + C_e^{F\downarrow}$ is the total electronic heat capacity of F. The pump action is modeled as $\Delta\dot{E}^F|_{\rm pump} = C_e^F\Delta\tilde{T}_{e0}\delta(t)$. To describe electron-phonon relaxation, we neglect spin flips and use [88]

$$\Delta\dot{E}^F|_{\rm ep} \propto \sum_\sigma\int d\delta\,(\alpha^2F)^{F\sigma}(\delta)\int d\epsilon\,\{[n^{F\sigma}(\epsilon) - n^{F\sigma}(\epsilon+\delta)]p^F(\delta) - [1 - n^{F\sigma}(\epsilon)]n^{F\sigma}(\epsilon+\delta)\}. \quad \text{(C2)}$$

Here, $(\alpha^2F)^{F\sigma}(\delta)$ denotes the Eliashberg function that describes the coupling of phonons of energy δ with two electronic states of the same spin σ and energy ϵ and $\epsilon + \delta$. The occupation number of the phonons is given by $p(\delta)$. Note that the term under the ϵ integral becomes zero for all δ and ϵ, if $n^{F\sigma}$ is a Fermi-Dirac distribution and p is a Bose-Einstein distribution with the same temperature.

b. Linear regime

We follow Ref. [13] and linearize Eq. (C2) with respect to $\Delta n^{F\sigma} = n^{F\sigma} - n_0$ and $\Delta p^F = p^F - p_0$ to obtain

$$\Delta \dot{E}^F|_{\mathrm{ep}} \propto \sum_\sigma \int d\delta \, (\alpha^2 F)^{F\sigma}(\delta)\delta \Delta p^F(\delta) - \sum_\sigma \int d\epsilon \, \Delta n^{F\sigma}(\epsilon) \int d\delta \, (\alpha^2 F)^{F\sigma}[1 - n_0(\epsilon - \delta) - n_0(\epsilon + \delta)]. \tag{C3}$$

Because the weight factor of $\Delta n^{F\sigma}(\epsilon)$ in Eq. (C3) is sufficiently smooth, it is legitimate to apply the moment expansion of Eq. (B13), resulting in [13]

$$\Delta \dot{E}^F|_{\mathrm{ep}} \propto \sum_\sigma \int d\delta \, (\alpha^2 F)^{F\sigma}(\delta)\delta \Delta p^F(\delta) - \Delta A^F \sum_\sigma \int d\delta \, (\alpha^2 F)^{F\sigma}(\delta)[-2n_0{}'(\mu_0 - \delta)]. \tag{C4}$$

The first integral approximately scales with the pump-induced phonon excess energy because $(\alpha^2 F)^{F\sigma}(\delta)$ is approximately proportional to the phonon density of states [88]. Owing to Eq. (B37), the second integral approximately scales with the excess energy of the F electrons. The generalized chemical potential does not show up in Eq. (C4), as the weight factor of $\Delta n^\sigma(\epsilon)$ in Eq. (C3) is antisymmetric with respect to $\epsilon - \mu_0$.

When we finally assume that the phonon distribution $p_0 + \Delta p$ is thermal and obeys Bose-Einstein statistics at temperature $T_0 + \Delta T_p^F$, Eq. (C4) leads to the familiar result [13]:

$$\Delta \dot{E}^F|_{\mathrm{ep}} = -G_{\mathrm{ep}}^F\left(\Delta \tilde{T}_e^F - \Delta T_p^F\right). \tag{C5}$$

Here, the coupling strength G_{ep}^F is proportional to $\sum_\sigma \int d\delta (\alpha^2 F)^{F\sigma}(\delta)[-2n_0{}'(\mu_0 - \delta)]$. In the last step to Eq. (C5), we took advantage of the fact that $\Delta \dot{E}^F|_{\mathrm{ep}} = 0$ when $\Delta \tilde{T}_e^F = \Delta T_p^F$. Equation (C5) is the generalization of the 2TM to nonthermal electron distributions in the linear excitation limit.

To close the system of equations, an equation of motion for the phonon temperature analogous to Eqs. (C1) and (C5) is given by

$$C_p^F \Delta \dot{T}_p^F = +G_{\mathrm{ep}}^F\left(\Delta \tilde{T}_e^F - \Delta T_p^F\right), \tag{C6}$$

where C_p^F is the phonon heat capacity of F.

2. 2TM for $F|N$ stack

To model the decay of the electronic excess heat in the $F|N$ stack, we assume that equilibration between electron baths of different spins and in different layers is much faster than electron-phonon equilibration. Therefore, all electron baths $X\sigma$ can be described by one common generalized excess temperature $\Delta \tilde{T}_e = \Delta \tilde{T}^{X\sigma}$. The phonon bath of each layer couples to the electrons of the same layer. Direct coupling of phonons between F and N is neglected. The energy-flow diagram, the differential equations [analogous to Eqs. (C1), (C5), and (C6)], and their solution are detailed in Supplemental Note 2 [72].

We find that, for the timescales relevant to our experiment, the dynamics of the generalized electron excess temperature is given by Eq. (B42), with

$$\Gamma_{\mathrm{ep}} = \frac{G_{\mathrm{ep}}^F + G_{\mathrm{ep}}^N}{C_e^F + C_e^N}, \tag{C7}$$

and

$$R = \frac{C_e^F + C_e^N}{C_e^F + C_e^N + C_p^F + C_p^N}. \tag{C8}$$

Here, C_e^X and C_p^X are the heat capacities of electrons and phonons in X, respectively, and G_{ep}^X quantifies electron-phonon coupling in X. For an F sample, the parameters Γ_{ep} and R are obtained by setting $C_e^N = 0$ and $G_{\mathrm{ep}}^N = 0$ in Eqs. (C7) and (C8).

Note that C_e^X, C_p^X, and G_{ep}^X are extensive quantities because they refer to the F and N volumes that are effectively coupled to each other in terms of ultrafast energy exchange. For our stack geometry, we assume equal coupling lengths into the depth of F and N. Therefore, we can replace the extrinsic quantities C_e^X, C_p^X, and G_{ep}^X by their specific (volume-normalized) counterparts, which can be obtained from the literature (see Table S1 [72]).

[1] E. Y. Vedmedenko, R. K. Kawakami, D. D. Sheka, P. Gambardella, A. Kirilyuk, A. Hirohata, C. Binek, O. Chubykalo-Fesenko, S. Sanvito, B. J. Kirby *et al.*, The 2020 magnetism roadmap, J. Phys. D. Appl. Phys. **53**, 453001 (2020).

[2] A. Kirilyuk, A. V Kimel, and T. Rasing, Ultrafast optical manipulation of magnetic order, Rev. Mod. Phys. **82**, 2731 (2010).

[3] A. Kirilyuk, A. V. Kimel, and T. Rasing, Laser-induced magnetization dynamics and reversal in ferrimagnetic alloys, Reports Prog. Phys. **76**, 26501 (2013).

[4] J. Walowski and M. Münzenberg, Perspective: ultrafast magnetism and THz spintronics, J. Appl. Phys. **120**, 140901 (2016).

[5] G. Malinowski, N. Bergeard, M. Hehn, and S. Mangin, Hot-electron transport and ultrafast magnetization dynamics in magnetic multilayers and nanostructures following femtosecond laser pulse excitation, Eur. Phys. J. B **91**, 98 (2018).

[6] A. El-Ghazaly, J. Gorchon, R. B. Wilson, A. Pattabi, and J. Bokor, Progress towards ultrafast spintronics applications, J. Magn. Magn. Mater. **502**, 166478 (2020).

[7] A. Eschenlohr, Spin dynamics at interfaces on femtosecond timescales, J. Phys. Condens. Matter **33**, 13001 (2020).

[8] E. Beaurepaire, J.-C. Merle, A. Daunois, and J.-Y. Bigot, Ultrafast Spin Dynamics in Ferromagnetic Nickel, Phys. Rev. Lett. **76**, 4250 (1996).

[9] J. Hohlfeld, E. Matthias, R. Knorren, and K. H. Bennemann, Nonequilibrium Magnetization Dynamics of Nickel, Phys. Rev. Lett. **78**, 4861 (1997).

[10] B. Koopmans, G. Malinowski, F. Dalla Longa, D. Steiauf, M. Fähnle, T. Roth, M. Cinchetti, and M. Aeschlimann, Explaining the paradoxical diversity of ultrafast laser-induced demagnetization, Nat. Mater. **9**, 259 (2010).

[11] R. B. Wilson, Y. Yang, J. Gorchon, C.-H. Lambert, S. Salahuddin, and J. Bokor, Electric current induced ultrafast demagnetization, Phys. Rev. B **96**, 045105 (2017).

[12] T. Roth, A. J. Schellekens, S. Alebrand, O. Schmitt, D. Steil, B. Koopmans, M. Cinchetti, and M. Aeschlimann, Temperature Dependence of Laser-Induced Demagnetization in Ni: A Key for Identifying the Underlying Mechanism, Phys. Rev. X **2**, 021006 (2012).

[13] A. L. Chekhov, Y. Behovits, J. J. F. Heitz, C. Denker, D. A. Reiss, M. Wolf, M. Weinelt, P. W. Brouwer, M. Münzenberg, and T. Kampfrath, Ultrafast Demagnetization of Iron Induced by Optical Versus Terahertz Pulses, Phys. Rev. X **11**, 041055 (2021).

[14] M. Stiehl, M. Weber, C. Seibel, J. Hoefer, S. T. Weber, D. M. Nenno, H. C. Schneider, B. Rethfeld, B. Stadtmüller, and M. Aeschlimann, Role of primary and secondary processes in the ultrafast spin dynamics of nickel, Appl. Phys. Lett. **120**, 62410 (2022).

[15] C. Dornes, Y. Acremann, M. Savoini, M. Kubli, M. J. Neugebauer, E. Abreu, L. Huber, G. Lantz, C. A. F. Vaz, H. Lemke *et al.*, The ultrafast Einstein–de Haas effect, Nature (London) **565**, 209 (2019).

[16] S. R. Tauchert, M. Volkov, D. Ehberger, D. Kazenwadel, M. Evers, H. Lange, A. Donges, A. Book, W. Kreuzpaintner, U. Nowak *et al.*, Polarized phonons carry angular momentum in ultrafast demagnetization, Nature (London) **602**, 73 (2022).

[17] K. Carva, M. Battiato, and P. M. Oppeneer, *Ab Initio* Investigation of the Elliott-Yafet Electron-Phonon Mechanism in Laser-Induced Ultrafast Demagnetization, Phys. Rev. Lett. **107**, 207201 (2011).

[18] B. Y. Mueller, A. Baral, S. Vollmar, M. Cinchetti, M. Aeschlimann, H. C. Schneider, and B. Rethfeld, Feedback Effect During Ultrafast Demagnetization Dynamics in Ferromagnets, Phys. Rev. Lett. **111**, 167204 (2013).

[19] A. Manchon, Q. Li, L. Xu, and S. Zhang, Theory of laser-induced demagnetization at high temperatures, Phys. Rev. B **85**, 064408 (2012).

[20] E. G. Tveten, A. Brataas, and Y. Tserkovnyak, Electron-magnon scattering in magnetic heterostructures far out of equilibrium, Phys. Rev. B **92**, 180412(R) (2015).

[21] M. Beens, R. A. Duine, and B. Koopmans, *s-d* model for local and nonlocal spin dynamics in laser-excited magnetic heterostructures, Phys. Rev. B **102**, 054442 (2020).

[22] M. Beens, R. A. Duine, and B. Koopmans, Modeling ultrafast demagnetization and spin transport: the interplay of spin-polarized electrons and thermal magnons, Phys. Rev. B **105**, 144420 (2022).

[23] W. Töws and G. M. Pastor, Many-Body Theory of Ultrafast Demagnetization and Angular Momentum Transfer in Ferromagnetic Transition Metals, Phys. Rev. Lett. **115**, 217204 (2015).

[24] K. Krieger, J. K. Dewhurst, P. Elliott, S. Sharma, and E. K. U. Gross, Laser-induced demagnetization at ultrashort time scales: predictions of TDDFT, J. Chem. Theory Comput. **11**, 4870 (2015).

[25] G. Malinowski, F. Dalla Longa, J. H. H. Rietjens, P. V. Paluskar, R. Huijink, H. J. M. Swagten, and B. Koopmans, Control of speed and efficiency of ultrafast demagnetization by direct transfer of spin angular momentum, Nat. Phys. **4**, 855 (2008).

[26] D. Rudolf, C. La-o-vorakiat, M. Battiato, R. Adam, J. M. Shaw, E. Turgut, P. Maldonado, S. Mathias, P. Grychtol, H. T. Nembach *et al.*, Ultrafast magnetization enhancement in metallic multilayers driven by superdiffusive spin current, Nat. Commun. **3**, 1037 (2012).

[27] A. Eschenlohr, M. Battiato, P. Maldonado, N. Pontius, T. Kachel, K. Holldack, R. Mitzner, A. Föhlisch, P. M. Oppeneer, and C. Stamm, Ultrafast spin transport as key to femtosecond demagnetization, Nat. Mater. **12**, 332 (2013).

[28] T. Kampfrath, M. Battiato, P. Maldonado, G. Eilers, J. Nötzold, S. Mährlein, V. Zbarsky, F. Freimuth, Y. Mokrousov, S. Blügel *et al.*, Terahertz spin current pulses controlled by magnetic heterostructures, Nat. Nanotechnol. **8**, 256 (2013).

[29] E. Turgut, C. La-o-vorakiat, J. M. Shaw, P. Grychtol, H. T. Nembach, D. Rudolf, R. Adam, M. Aeschlimann, C. M. Schneider, T. J. Silva *et al.*, Controlling the Competition between Optically Induced Ultrafast Spin-Flip Scattering and Spin Transport in Magnetic Multilayers, Phys. Rev. Lett. **110**, 197201 (2013).

[30] J. Chen, U. Bovensiepen, A. Eschenlohr, T. Müller, P. Elliott, E. K. U. Gross, J. K. Dewhurst, and S. Sharma, Competing Spin Transfer and Dissipation at Co/Cu(001) Interfaces on Femtosecond Timescales, Phys. Rev. Lett. **122**, 067202 (2019).

[31] A. Alekhin, I. Razdolski, N. Ilin, J. P. Meyburg, D. Diesing, V. Roddatis, I. Rungger, M. Stamenova, S. Sanvito, U. Bovensiepen *et al.*, Femtosecond Spin Current Pulses Generated by the Nonthermal Spin-Dependent Seebeck Effect and Interacting with Ferromagnets in Spin Valves, Phys. Rev. Lett. **119**, 017202 (2017).

[32] I. Razdolski, A. Alekhin, N. Ilin, J. P. Meyburg, V. Roddatis, D. Diesing, U. Bovensiepen, and A. Melnikov, Nanoscale interface confinement of ultrafast spin transfer torque driving non-uniform spin dynamics, Nat. Commun. **8**, 15007 (2017).

[33] M. L. M. Lalieu, R. Lavrijsen, R. A. Duine, and B. Koopmans, Investigating optically excited terahertz standing spin waves using noncollinear magnetic bilayers, Phys. Rev. B **99**, 184439 (2019).

[34] T. Seifert, S. Jaiswal, U. Martens, J. Hannegan, L. Braun, P. Maldonado, F. Freimuth, A. Kronenberg, J. Henrizi, and I. Radu, Efficient metallic spintronic emitters of ultrabroadband terahertz radiation, Nat. Photonics **10**, 483 (2016).

[35] D. Yang, J. Liang, C. Zhou, L. Sun, R. Zheng, S. Luo, Y. Wu, and J. Qi, Powerful and tunable THz emitters based on the Fe/Pt magnetic heterostructure, Adv. Opt. Mater. **4**, 1944 (2016).

[36] Y. Wu, M. Elyasi, X. Qiu, M. Chen, Y. Liu, L. Ke, and H. Yang, High-performance THz emitters based on ferromagnetic/nonmagnetic heterostructures, Adv. Mater. **29**, 1603031 (2017).

[37] G. Torosyan, S. Keller, L. Scheuer, R. Beigang, and E. T. Papaioannou, Optimized spintronic terahertz emitters based on epitaxial grown Fe/Pt layer structures, Sci. Rep. **8**, 1311 (2018).

[38] R. Schneider, M. Fix, R. Heming, S. Michaelis de Vasconcellos, M. Albrecht, and R. Bratschitsch, Magnetic-field-dependent THz emission of spintronic TbFe/Pt layers, ACS Photonics **5**, 3936 (2018).

[39] M. Meinert, B. Gliniors, O. Gueckstock, T. S. Seifert, L. Liensberger, M. Weiler, S. Wimmer, H. Ebert, and T. Kampfrath, High-Throughput Techniques for Measuring the Spin Hall Effect, Phys. Rev. Appl. **14**, 064011 (2020).

[40] T. S. Seifert, N. M. Tran, O. Gueckstock, S. M. Rouzegar, L. Nadvornik, S. Jaiswal, G. Jakob, V. V. Temnov, M. Münzenberg, M. Wolf *et al.*, Terahertz spectroscopy for all-optical spintronic characterization of the spin-Hall-effect metals Pt, W and $Cu_{80}Ir_{20}$, J. Phys. D. Appl. Phys. **51**, 364003 (2018).

[41] M. B. Jungfleisch, Q. Zhang, W. Zhang, J. E. Pearson, R. D. Schaller, H. Wen, and A. Hoffmann, Control of Terahertz Emission by Ultrafast Spin-Charge Current Conversion at Rashba Interfaces, Phys. Rev. Lett. **120**, 207207 (2018).

[42] E. T. Papaioannou and R. Beigang, THz spintronic emitters: a review on achievements and future challenges, Nanophotonics **10**, 1243 (2021).

[43] Z. Feng, H. Qiu, D. Wang, C. Zhang, S. Sun, B. Jin, and W. Tan, Spintronic terahertz emitter, J. Appl. Phys. **129**, 10901 (2021).

[44] C. Bull, S. M. Hewett, R. Ji, C.-H. Lin, T. Thomson, D. M. Graham, and P. W. Nutter, Spintronic terahertz emitters: status and prospects from a materials perspective, APL Mater. **9**, 90701 (2021).

[45] W. Wu, C. Yaw Ameyaw, M. F. Doty, and M. B. Jungfleisch, Principles of spintronic THz emitters, J. Appl. Phys. **130**, 91101 (2021).

[46] T. S. Seifert, L. Cheng, Z. Wei, T. Kampfrath, and J. Qi, Spintronic sources of ultrashort terahertz electromagnetic pulses, Appl. Phys. Lett. **120**, 180401 (2022).

[47] T. Vogel, A. Omar, S. Mansourzadeh, F. Wulf, N. Martín Sabanés, M. Müller, T. S. Seifert, A. Weigel, G. Jakob, M. Kläui *et al.*, Average power scaling of THz spintronic emitters in reflection geometry, Opt. Express **30**, 20451 (2022).

[48] N. Laman, M. Bieler, and H. Van Driel, Ultrafast shift and injection currents observed in wurtzite semiconductors via emitted terahertz radiation, J. Appl. Phys. **98**, 103507 (2005).

[49] F. Nastos and J. E. Sipe, Optical rectification and shift currents in GaAs and GaP response: Below and above the band gap, Phys. Rev. B **74**, 035201 (2006).

[50] F. Nastos and J. E. Sipe, Optical rectification and current injection in unbiased semiconductors, Phys. Rev. B **82**, 235204 (2010).

[51] J. L. Cabellos, B. S. Mendoza, and A. I Shkrebtii, Optical coherent current control at surfaces: Theory of injection current, Phys. Rev. B **84**, 195326 (2011).

[52] L. Braun, G. Mussler, A. Hruban, M. Konczykowski, T. Schumann, M. Wolf, M. Münzenberg, L. Perfetti, and T. Kampfrath, Ultrafast photocurrents at the surface of the three-dimensional topological insulator Bi_2Se_3, Nat. Commun. **7**, 13259 (2016).

[53] J. K. Dewhurst, P. Elliott, S. Shallcross, E. K. U. Gross, and S. Sharma, Laser-Induced intersite spin transfer, Nano Lett. **18**, 1842 (2018).

[54] F. Siegrist, J. A. Gessner, M. Ossiander, C. Denker, Y.-P. Chang, M. C. Schröder, A. Guggenmos, Y. Cui, J. Walowski, U. Martens *et al.*, Light-wave dynamic control of magnetism, Nature (London) **571**, 240 (2019).

[55] M. Hofherr, S. Häuser, J. K. Dewhurst, P. Tengdin, S. Sakshath, H. T. Nembach, S. T. Weber, J. M. Shaw, T. J. Silva, H. C. Kapteyn *et al.*, Ultrafast optically induced spin transfer in ferromagnetic alloys, Sci. Adv. **6**, eaay8717 (2020).

[56] F. Willems, C. T. L. Smeenk, N. Zhavoronkov, O. Kornilov, I. Radu, M. Schmidbauer, M. Hanke, C. von Korff Schmising, M. J. J. Vrakking *et al.*, Probing ultrafast spin dynamics with high-harmonic magnetic circular dichroism spectroscopy, Phys. Rev. B **92**, 220405(R) (2015).

[57] D. Steil, J. Walowski, F. Gerhard, T. Kiessling, D. Ebke, A. Thomas, T. Kubota, M. Oogane, Y. Ando, J. Otto *et al.*, Efficiency of ultrafast optically induced spin transfer in heusler compounds, Phys. Rev. Res. **2**, 023199 (2020).

[58] M. Battiato, K. Carva, and P. M. Oppeneer, Superdiffusive Spin Transport As a Mechanism of Ultrafast Demagnetization, Phys. Rev. Lett. **105**, 027203 (2010).

[59] D. M. Nenno, S. Kaltenborn, and H. C. Schneider, Boltzmann transport calculation of collinear spin transport on short timescales, Phys. Rev. B **94**, 115102 (2016).

[60] J. Hurst, P.-A. Hervieux, and G. Manfredi, Spin current generation by ultrafast laser pulses in ferromagnetic nickel films, Phys. Rev. B **97**, 014424 (2018).

[61] K. Bühlmann, G. Saerens, A. Vaterlaus, and Y. Acremann, Detection of femtosecond spin voltage pulses in a thin iron film, Struct. Dyn. **7**, 65101 (2020).

[62] O. Gueckstock, L. Nádvorník, M. Gradhand, T. S. Seifert, G. Bierhance, R. Rouzegar, M. Wolf, M. Vafaee, J. Cramer, M. A. Syskaki *et al.*, Terahertz spin-to-charge conversion by interfacial skew scattering in metallic bilayers, Adv. Mater. **33**, 2006281 (2021).

[63] T. J. Huisman, R. V. Mikhaylovskiy, J. D. Costa, F. Freimuth, E. Paz, J. Ventura, P. P. Freitas, S. Blügel, Y. Mokrousov, T. Rasing *et al.*, Femtosecond control of electric currents in metallic ferromagnetic heterostructures, Nat. Nanotechnol. **11**, 455 (2016).

[64] G. E. W. Bauer, E. Saitoh, and B. J. van Wees, Spin caloritronics, Nat. Mater. **11**, 391 (2012).

[65] A. Fognini, T. U. Michlmayr, A. Vaterlaus, and Y. Acremann, Laser-induced ultrafast spin current pulses: A thermodynamic approach, J. Phys. Condens. Matter **29**, 214002 (2017).

[66] G.-M. Choi, C.-H. Moon, B.-C. Min, K.-J. Lee, and D. G. Cahill, Thermal spin-transfer torque driven by the spin-dependent Seebeck effect in metallic spin-valves, Nat. Phys. **11**, 576 (2015).

[67] B. Y. Mueller, T. Roth, M. Cinchetti, M. Aeschlimann, and B. Rethfeld, Driving force of ultrafast magnetization dynamics, New J. Phys. **13**, 123010 (2011).

[68] B. Y. Mueller and B. Rethfeld, Thermodynamic μT model of ultrafast magnetization dynamics, Phys. Rev. B **90**, 144420 (2014).

[69] G.-M. Choi, B.-C. Min, K.-J. Lee, and D. G. Cahill, Spin current generated by thermally driven ultrafast demagnetization, Nat. Commun. **5**, 4334 (2014).

[70] T. Lichtenberg, M. Beens, M. H. Jansen, B. Koopmans, and R. A. Duine, Probing optically induced spin currents using terahertz spin waves in noncollinear magnetic bilayers, Phys. Rev. B **105**, 144416 (2022).

[71] S. Mathias, C. La-O-Vorakiat, P. Grychtol, P. Granitzka, E. Turgut, J. M. Shaw, R. Adam, H. T. Nembach, M. E. Siemens, S. Eich *et al.*, Probing the timescale of the exchange interaction in a ferromagnetic alloy, Proc. Natl. Acad. Sci. USA **109**, 4792 (2012).

[72] See Supplemental Material at http://link.aps.org/supplemental/10.1103/PhysRevB.106.144427 for more data and more details on experimental procedures and modeling.

[73] E. Beaurepaire, G. M. Turner, S. M. Harrel, M. C. Beard, J.-Y. Bigot, and C. A. Schmuttenmaer, Coherent terahertz emission from ferromagnetic films excited by femtosecond laser pulses, Appl. Phys. Lett. **84**, 3465 (2004).

[74] W. Zhang, P. Maldonado, Z. Jin, T. S. Seifert, J. Arabski, G. Schmerber, E. Beaurepaire, M. Bonn, T. Kampfrath, P. M. Oppeneer *et al.*, Ultrafast terahertz magnetometry, Nat. Commun. **11**, 4247 (2020).

[75] J. M. Schleicher, S. M. Harrel, C. A. Schmuttenmaer, E. Beaurepaire, and J.-Y. Bigot, Characterization of magnetization dynamics using terahertz emission spectroscopy, in *15th International Conference on Ultrafast Phenomena* (Optica Publishing Group, Pacific Grove, 2006), p. TuH8.

[76] T. J. Huisman, R. V. Mikhaylovskiy, A. Tsukamoto, Th. Rasing, and A. V. Kimel, Simultaneous measurements of terahertz emission and magneto-optical kerr effect for resolving ultrafast laser-induced demagnetization dynamics, Phys. Rev. B **92**, 104419 (2015).

[77] T. S. Seifert, U. Martens, F. Radu, M. Ribow, M. Berritta, L. Nádvorník, R. Starke, T. Jungwirth, M. Wolf, I. Radu *et al.*, Frequency-independent terahertz anomalous Hall effect in $DyCo_5$, $Co_{32}Fe_{68}$, and $Gd_{27}Fe_{73}$ thin films from DC to 40 THz, Adv. Mater. **33**, 2007398 (2021).

[78] Q. Wu and X.-C. Zhang, Free-space electro-optics sampling of mid-infrared pulses, Appl. Phys. Lett. **71**, 1285 (1997).

[79] A. Leitenstorfer, S. Hunsche, J. Shah, M. C. Nuss, and W. H. Knox, Detectors and sources for ultrabroadband electro-optic sampling: experiment and theory, Appl. Phys. Lett. **74**, 1516 (1999).

[80] T. Kampfrath, J. Nötzold, and M. Wolf, Sampling of broadband terahertz pulses with thick electro-optic crystals, Appl. Phys. Lett. **90**, 231113 (2007).

[81] M. Porer, J.-M. Ménard, and R. Huber, Shot noise reduced terahertz detection via spectrally postfiltered electro-optic sampling, Opt. Lett. **39**, 2435 (2014).

[82] T. S. Seifert, S. Jaiswal, J. Barker, S. T. Weber, I. Razdolski, J. Cramer, O. Gueckstock, S. F. Maehrlein, L. Nadvornik, S. Watanabe *et al.*, Femtosecond formation dynamics of the spin Seebeck effect revealed by terahertz spectroscopy, Nat. Commun. **9**, 2899 (2018).

[83] G. Ramakrishnan, R. Chakkittakandy, and P. C. M. Planken, Terahertz generation from graphite, Opt. Express **17**, 16092 (2009).

[84] Q. Zhang, Z. Luo, H. Li, Y. Yang, X. Zhang, and Y. Wu, Terahertz Emission from Anomalous Hall Effect in a Single-Layer Ferromagnet, Phys. Rev. Appl. **12**, 054027 (2019).

[85] C. A. Meserole, G. L. Fisher, D. J. Hilton, R. D. Averitt, D. J. Funk, and A. J. Taylor, Growth of thin Fe(001) films for terahertz emission experiments, Appl. Surf. Sci. **253**, 6992 (2007).

[86] W. Nolting and A. Ramakanth, *Quantum Theory of Magnetism* (Springer-Verlag, Berlin, Heidelberg, 2009).

[87] J. Stöhr and H. C. Siegmann, *Magnetism: From Fundamentals to Nanoscale Dynamics* (Springer, Berlin, Heidelberg, 2006).

[88] P. B. Allen, Theory of Thermal Relaxation of Electrons in Metals, Phys. Rev. Lett. **59**, 1460 (1987).

[89] J. Hohlfeld, S.-S. Wellershoff, J. Güdde, U. Conrad, V. Jähnke, and E. Matthias, Electron and lattice dynamics following optical excitation of metals, Chem. Phys. **251**, 237 (2000).

[90] W. He, T. Zhu, X.-Q. Zhang, H.-T. Yang, and Z.-H. Cheng, Ultrafast demagnetization enhancement in CoFeB/MgO/CoFeB magnetic tunneling junction driven by spin tunneling current, Sci. Rep. **3**, 2883 (2013).

[91] S. R. Boona, R. C. Myers, and J. P. Heremans, Spin caloritronics, Energy Environ. Sci. **7**, 885 (2014).

[92] S. Eich, M. Plötzing, M. Rollinger, S. Emmerich, R. Adam, C. Chen, H. C. Kapteyn, M. M. Murnane, L. Plucinski, D. Steil *et al.*, Band structure evolution during the ultrafast ferromagnetic paramagnetic phase transition in cobalt, Sci. Adv. **3**, e1602094 (2017).

[93] T. J. Huisman, C. Ciccarelli, A. Tsukamoto, R. V. Mikhaylovskiy, T. Rasing, and A. V. Kimel, Spin-photocurrents generated by femtosecond laser pulses in a ferrimagnetic GdFeCo/Pt bilayer, Appl. Phys. Lett. **110**, 72402 (2017).

[94] S. F. Maehrlein, I. Radu, P. Maldonado, A. Paarmann, M. Gensch, A. M. Kalashnikova, R. V. Pisarev, M. Wolf, P. M. Oppeneer, J. Barker *et al.*, Dissecting spin-phonon equilibration in ferrimagnetic insulators by ultrafast lattice excitation, Sci. Adv. **4**, eaar5164 (2018).

[95] A. Grechnev, I. Di Marco, M. I. Katsnelson, A. I. Lichtenstein, J. Wills, and O. Eriksson, Theory of bulk and surface quasiparticle spectra for Fe, Co, and Ni, Phys. Rev. B **76**, 035107 (2007).

[96] R. Freeman, A. Zholud, Z. Dun, H. Zhou, and S. Urazhdin, Evidence for Dyakonov-Perel-Like Spin Relaxation in Pt, Phys. Rev. Lett. **120**, 067204 (2018).

[97] W. Hoppe, J. Weber, S. Tirpanci, O. Gueckstock, T. Kampfrath, and G. Woltersdorf, On-chip generation of ultrafast current pulses by nanolayered spintronic terahertz emitters, ACS Appl. Nano Mater. **4**, 7454 (2021).

[98] M. A. Wahada, E. Şaşıoğlu, W. Hoppe, X. Zhou, H. Deniz, R. Rouzegar, T. Kampfrath, I. Mertig, S. S. P. Parkin, and G. Woltersdorf, Atomic scale control of spin current transmission at interfaces, Nano Lett. **22**, 3539 (2022).

[99] B. F. Miao, S. Y. Huang, D. Qu, and C. L. Chien, Inverse Spin Hall Effect in a Ferromagnetic Metal, Phys. Rev. Lett. **111**, 066602 (2013).

[100] F. N. Kholid, D. Hamara, M. Terschanski, F. Mertens, D. Bossini, M. Cinchetti, L. McKenzie-Sell, J. Patchett, D. Petit,

R. Cowburn, J. Robinson, J. Barker, and C. Ciccarelli, Temperature dependence of the picosecond spin seebeck effect, Appl. Phys. Lett. **119**, 32401 (2021).

[101] W.-T. Lu, Y. Zhao, M. Battiato, Y. Wu, and Z. Yuan, Interface reflectivity of a superdiffusive spin current in ultrafast demagnetization and terahertz emission, Phys. Rev. B **101**, 014435 (2020).

[102] A. Kirihara, K. Uchida, Y. Kajiwara, M. Ishida, Y. Nakamura, T. Manako, E. Saitoh, and S. Yorozu, Spin-current-driven thermoelectric coating, Nat. Mater. **11**, 686 (2012).